日本磁気学会
ISSN 2432-0250
Journal of the Magnetics Society of Japan
Electronic Journal URL: https://www.jstage.jst.go.jp/browse/msjmag

Vol.42 No.3 2018

Journal

JOURNAL OF THE MAGNETICS SOCIETY OF JAPAN

Vol.42 No.3 2018

日本磁気学会

ISSN 2432-0250

HP: http://www.magnetics.jp/ e-mail: msj@bj.wakwak.com

Electronic Journal: http://www.jstage.jst.go.jp/browse/msjmag

Journal of the Magnetics Society of Japan
Vol. 42, No. 3

Electronic Journal URL: https://www.jstage.jst.go.jp/browse/msjmag

CONTENTS

J. Magn. Soc. Jpn., **42**, 62-71 (2018)

<Paper>

Anisotropic Magnetic Core for the Iron Loss Reduction of Permanent Magnet Synchronous Motor

Nicolas Denis*, Shinya Takeda*, Kohei Fujitani*, Keisuke Fujisaki*, Shunya Odawara**

* Toyota Technological Institute, *2-12-1 Hisakata, Tempaku-ku, Nagoya 468-8511, Japan*

** Kitami Institute of Technology, *165 Koen-cho Kitami, Hokkaido 090-8507, Japan*

An interior permanent magnet synchronous motor (IPMSM) using a stator core made of grain-oriented (GO) anisotropic magnetic material is manufactured to evaluate the potential iron loss reduction that GO can bring compared to the conventionally used non-oriented (NO) quasi-isotropic silicon steel. The stator core is divided into yoke and teeth pieces that are arranged so that the GO material easy magnetization direction follows the main magnetic flux that flows in the core during the motor operation. The motor iron loss is measured under two conditions: 1) the IPMSM is rotated by an external motor ("drag force operation"), 2) the IPMSM is driven by a pulse-width modulation (PWM) inverter without load ("no-load operation"). The manufactured motor shows 13.5 % iron loss reduction during drag force operation and 5 % reduction during no-load operation. Numerical calculation is also carried out by 2-D finite element analysis (FEA) to confirm the experimental data.

Key words: Grain-oriented magnetic material, Iron losses, Magnetic core, Permanent magnet synchronous motor, Silicon steel

1. Introduction

Global warming and/or polluted urban areas is one of the biggest challenge that the society is facing today. Electrified vehicles are presented as one of the possible solutions but they still have to be more affordable and increase their autonomy in order to be more widely accepted by the society. The limited embeddable electrical energy in batteries is still a strong limit and therefore, the losses that occur in each part of the electrical powertrains should be reduced as much as possible. Interior permanent magnet synchronous motors (IPMSM) are known to be very efficient driving power sources for electrical vehicles but still contribute to waste of electrical energy caused by mechanical friction loss, coper loss and iron loss. In order to reduce the iron loss, focusing on the magnetic materials characteristics and applications is important [1].

Non-oriented silicon steel (NO) has small magnetic anisotropy. Moreover, its iron loss density and its magnetization characteristic are usually measured using the Epstein frame in which several sheets are superimposed with alternating direction (90°, 0°). In this way, the measured characteristic is considered as an average characteristic over the sheet orientation angle range. In other words, knowing the fact that the anisotropy is usually small, one single average characteristic is usually preferred for simplification rather that a complete characterization for every orientation angle. On the other hand, grain-oriented steel (GO) [2-3] has strong magnetic anisotropy [4] that has to be measured and characterized. GO is generally used for electrical transformer cores. It has very small iron loss density in its easy magnetization direction.

Fig. 1 shows the magnetic characteristics of NO and GO at 50 Hz taken from catalogue data [5]. The NO steel has one single characteristic, as explained previously, while the GO steel characteristic depends on the angle φ, which is the angle between the magnetic flux density vector and the easy magnetization direction. In particular, GO has low iron loss density in the easy magnetization axis ($\varphi = 0°$, (100) direction) while high in the transverse direction ($\varphi = 90°$, (010) direction).

Because the magnetic flux in a stator core of an electrical motor flows multi directionally, simply substituting NO steel by GO steel would make the magnetic flux force its way through the transverse direction of GO at some parts. This would have for consequence to likely increase the iron losses. This underlines the challenge of designing and manufacturing a motor core with GO steel. However, considering its superior magnetic properties, the authors think that GO is worth experimental trials in scientific research.

A proposed solution is to assemble the stator shifting each lamination from the previous one with a constant angle, so the easy magnetization direction appears in different parts of the stator [6]. This supposedly makes the magnetic flux pass from one lamination to another in order to avoid the parts which present the transverse magnetization direction. However, it can be argued that the magnetic flux could be restrained, causing a loss of performance of the motor. Moreover, in ref. 6), tests are done using the stator as a transformer core and not as part of an actual motor. Consequently, segmented type stators are tried in which teeth and yoke are divided [7-9], however only the teeth are made of GO steel. It would be interesting to evaluate the improvement of a stator composed solely of GO steel. GO steel is also applied to rotor cores [10-13] for which increase of electromagnetic torque and efficiency are reported. However, the rotor core is usually not the major contributor of the motor iron losses, so for the purpose of iron loss reduction, studies and trials should focus primarily on the stator.

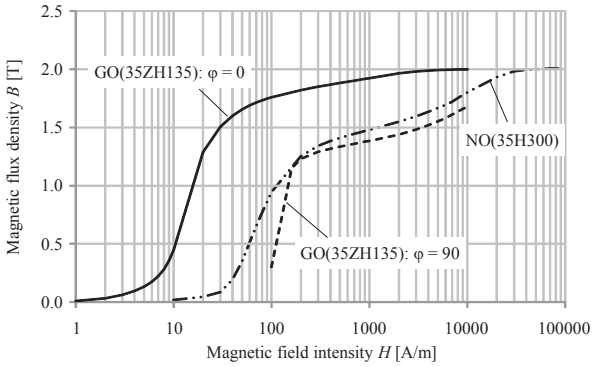

(a) *B-H* curve

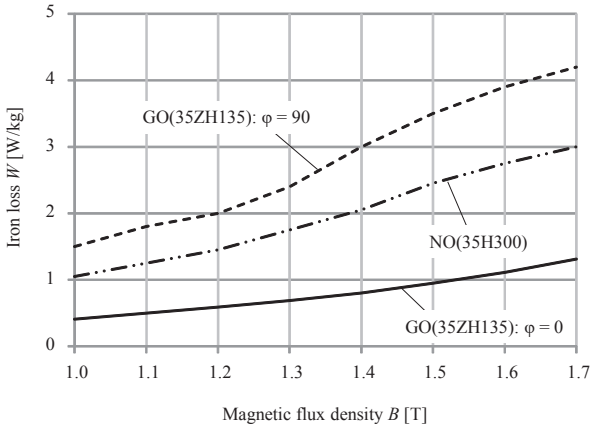

(b) *B-W* curve

Fig. 1 Magnetic characteristics of NO steel (35H300) and GO steel (35ZH135) at 50 Hz.

Considering the current state of the art described above, this paper proposes a novel assembly for an IPMSM stator core made completely of GO steel. The IPMSM using the proposed stator core, illustrated in Fig. 2, will be called "magnetic anisotropic motor" hereafter. The considerations lying under the proposed core assembly are as follows: at first, the assumption that the magnetic flux flows mainly in the radial direction in the stator tooth and in the tangential direction in the stator yoke is made. Based on this assumption, it is proposed to divide the yoke part and tooth part and cut GO steel pieces accordingly. The GO steel pieces are then arranged so that the GO easy magnetization direction coincides mostly with the tangential direction in the yoke and, similarly, the GO easy magnetization direction coincides mostly with the radial direction in the teeth. This configuration has been chosen as an attempt to maximize the correspondence between the magnetic flux direction and the GO easy magnetization direction. In previous works, the suitable shape of the proposed magnetic anisotropic motor was designed by using finite element analysis (FEA) [14]. Iron loss measurement trials have been made under "drag force operation" (IPMSM rotated by an external motor) in the previous work [15] but it is believed that these measurements along with the analysis have to be corrected and improved. Moreover ref. 15) does not present any results concerning the motor rotated by a pulse-width modulation (PWM) inverter, which is the most common way to drive an IPMSM.

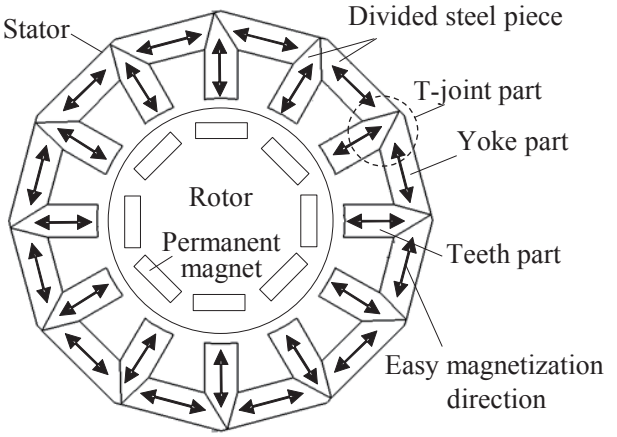

Fig. 2 Geometry of the proposed magnetic anisotropic motor.

In this paper, section II provides some important information about the manufacturing process. The manufacture of the stator core requires precision and limiting the mechanical stress as much as possible is crucial. In section III, the magnetic anisotropic motor is tested under both "drag force operation" and "no-load operation" (IPMSM driven by a PWM inverter without mechanical load) and its capacity to reduce iron loss is assessed. Finally, section IV presents numerical magnetic calculation to verify the measured data.

2. Trial Manufacture of Magnetic Anisotropic Motor

The GO steel 35ZH135 is used to manufacture the stator of an IPMSM with 12-slots, 8-poles, and concentrated windings. The detailed geometry is shown in Fig. 3 and Table I. In the proposed geometry, the slot opening is quite large and will cause a high torque ripple. Since no dedicated machinery was available to wind the stator, wide slot opening has been chosen to make the winding process easier to do by hand. Since the reduction of torque ripple is not the focus of this study, it is considered that this particular geometry does not negatively affect the conclusions of this paper.

For the sake of comparison, a stator made of NO steel 35H300 has also been manufactured. Since the manufacture process of the NO stator is significantly different from that of the GO stator, it is difficult to obtain geometrical similarity to the 10 microns order. The dimensions of the NO stator differ slightly from Table I. R_{Si} is equal to 38.20 mm and the axial length to 46.9 mm. It is thought that the differences observed do not influence the iron loss to the point at which a comparison is significantly unfair.

In both cases, the rotor core of the motor is made of NO steel (35H300). Sintered NdFeB permanent magnets (PM) are used. Their characteristics are given in Table II.

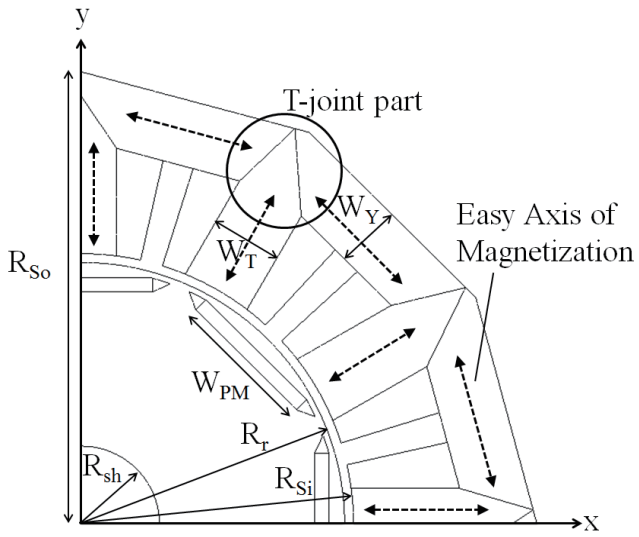

Fig. 3 Proposed magnetic anisotropic motor (quarter size model).

TABLE I SPECIFICATIONS OF MAGNETIC ANISOTROPIC MOTOR.

Number of poles	-	8
Number of slots	-	12
Radius of stator core (outside)	R_{So}	64 mm
Radius of stator core (inside)	R_{Si}	38.15 mm
Yoke width	W_Y	9.17 mm
Teeth width	W_T	10.00 mm
Radius of rotor	R_R	36.95 mm
Air gap between stator and rotor	G	1.20 mm
PM width	W_{PM}	20 mm
Stator axial length	-	47.0 mm
Winding method	-	Concentrated

In the GO stator core, the junction between the tooth part and the yoke parts is illustrated in Fig. 4. A joint structure without overlap from one layer to another, as in Fig. 4.a, would cause mechanical brittleness. Consequently, a structure with overlaps, as in Fig. 4.b, has been chosen to ensure the stator overall solidity. Therefore, the angle θ defined in Fig. 4.b has to be taken inferior to 90°. In the previous study [14], numerical analysis has been performed in order to find an angle θ that would ensure good tradeoff between iron loss minimization and mechanical solidity. The selected angle is 80°.

The manufacture process of the GO stator has been detailed in previous papers [14)-15)]. This paper does not aim at providing detailed manufacture explanations but some points should be noted. For both the GO and NO stators, wire electric discharge machining has been used to cut the electrical steel sheets while avoiding high mechanical stress [16)]. In order to improve the mechanical solidity of the GO stator, compressive force was applied for 30 minutes after each completed layer. As a consequence, the stacking factor of the GO stator is slightly higher (99.8%) than for the NO stator (97.7%). GO is known to have more stress sensitivity than NO

TABLE II CHARACTERISTICS OF PERMANENT MAGNETS AT ROOM TEMPERATURE.

PM residual magnetization	B_m	1.28 T
Coercive force	H_c	1.02×10^6 A/m
Electrical conductivity	σ	6.25×10^5 S/m

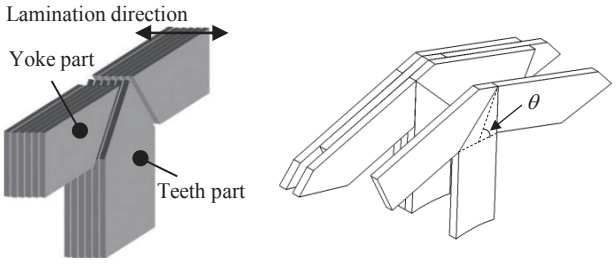

(a) No overlapping (b) Overlapping

Fig. 4 T-joint part, (a) No overlap, (b) With overlap.

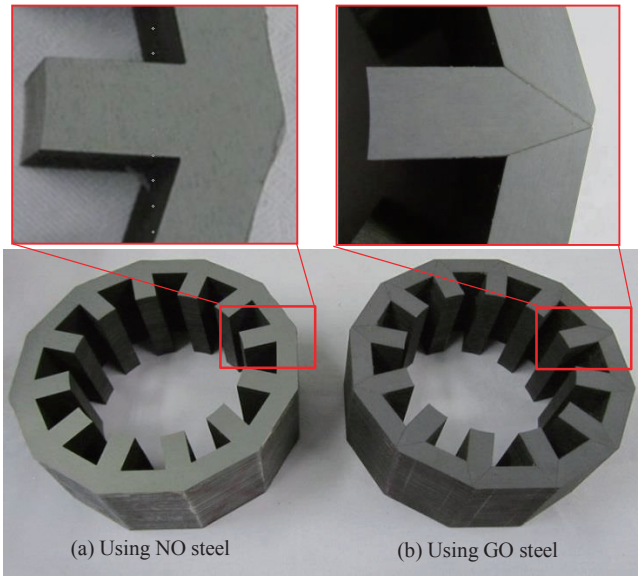

Fig. 5 Completed stator core specimens.

but the effect is negligible in case of uniform axial compression. Therefore, a jig[15)], which was manufactured so that a good geometrical accuracy can be kept, is prepared to avoid this type of stress. Fig. 5 shows the completed stator core specimens.

It can be understood that the GO requires extra manufacture because of the special junction between teeth parts and yoke parts. On top of that, GO requires more cutting using the rather expensive wire electric discharge machining. Therefore, the proposed GO stator core increases manufacture complexity and cost, which is a disadvantage compared to the NO stator. However, future development in manufacturing technology could help to overcome these problems. Moreover, as motor applications expand widely, the proposed GO stator core could be useful for special applications (like aircraft or spacecraft) in which the iron loss reduction is required while the motor core cost is less crucial.

3. Experimental Evaluation of Magnetic Anisotropic Motor

As explained in the introduction, the manufactured magnetic anisotropic motor iron losses are evaluated experimentally under "drag force operation" and "no-load operation". Table III shows equipment used for the operations. The tests are explained hereafter.

3.1 Drag Force Operation

The drag force operation measurement system is illustrated in Fig. 6. No current is supplied to the tested IPMSM (trial motor MS). The rotor of the IPMSM is rotated by an external brushless DC (BLDC) motor. The BLDC motor rotational speed ω and output torque T are measured by a revolution indicator and a torque meter, respectively. When the rotor is rotated by the BLDC motor, the rotating permanent magnets magnetize the stator core, which creates stator iron losses. The teeth shape of the IPMSM stator core generates variating magnetic flux density in the rotor and magnets which cause rotor and magnet iron losses.

Since no electrical power is supplied to the IPMSM, the output power supplied by the BLDC motor balances all the IPMSM losses, namely the iron loss W_{i_drag} and the mechanical friction loss W_m. Then the following equation holds.

$$P_{out} = \omega T = W_{i\_drag} + W_m, \quad (1)$$

where P_{out} is the BLDC motor output mechanical power.

In order to measure the mechanical loss, a rotor with demagnetized permanent magnets is used. It has the same shape and bearings as the rotor with magnetized permanent magnets. When the same drag force test as described above is carried out replacing the conventional rotor by the demagnetized rotor, there are no iron loss generation and the term W_i disappears in (1). Therefore, W_m can be calculated using the following equation.

$$P'_{out} = \omega T' = W_m, \quad (2)$$

where P'_{out} and T' are the BLDC motor output mechanical power and torque respectively, when the demagnetized rotor is used. The IPMSM iron losses under drag force operation can be deduced from (1) and (2).

The torque to measure is relatively small, which makes the measurements more susceptible to uncertainties. The torque meter chosen for the test can measure a maximum torque of 1 N·m and has an accuracy of ±2 mN·m, which corresponds to ±0.157 W at 750 rpm and ±0.628 W at 3000 rpm for the measured power accuracy. In order to improve the reliability of the results, the motor runs a first for 30 minutes at a given speed in order to reach thermal steady-state operation and avoid measurement differences due to thermal transient behavior. Then one measurement consists in recording the torque and speed for 20 seconds. The recorded data are then averaged over the 20 seconds time span. This procedure is done 10 times. The standard deviation of the 10 measurements is then calculated.

3.2 No-load Operation

During no-load operation, the trial IPMSM is driven by a 3-phase PWM inverter. As shown in Fig. 7, the inverter output power $P_{inverter}$ and the IPMSM phase RMS current I_n are measured using a power analyzer whose bandwidth is 2 MHz and sampling frequency 2.2 MHz. The rotational speed is controlled using a vector control scheme and a speed feedback provided by an encoder. The d-axis IPMSM phase current reference is set to zero, the PWM carrier frequency to 1 kHz and the DC bus voltage to 180 V.

Because the trial IPMSM has no mechanical load, the power balance verifies the following equation.

$$P_{inverter} = 3R_a I_n^2 + W_m + W_{enc} + W_{i\_inv}, \quad (3)$$

where R_a (0.510 Ω) is the phase resistance that has been measured in DC condition just after the measurements, W_{enc} is the mechanical loss of the encoder measured by the same method as used for the estimation of W_m. Then the IPMSM iron loss under no-load operation W_{i_inv} can be deduced.

The measurement procedure of ten consecutive trials introduced in the last section has also been carried out to increase the reliability of the measurements.

TABLE III EXPERIMENTAL EQUIPMENT.

Item	Model	Manufacturer
Torque meter	TH-3014H	Ono Sokki
Revolution indicator	MD-0118	Ono Sokki
Watt meter	TS-2800	Ono Sokki
Blushless DC motor	BXM6200-A	Oriental motor
Encoder	MES-20-1024	Microtech Laboratory
Power analyzer	PPA-5530	Iwatsu
PWM inverter	MWINV-9R122B	Myway Plus

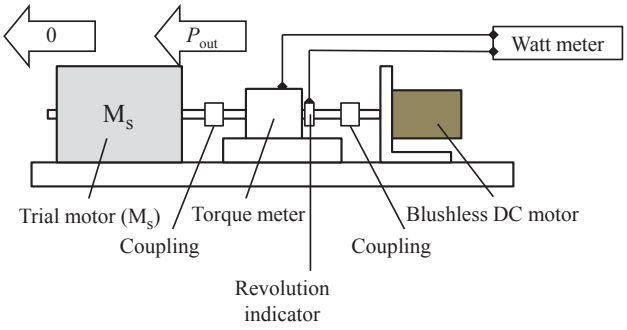

Fig. 6 Schematic diagram of the iron loss measurement system by drag force test.

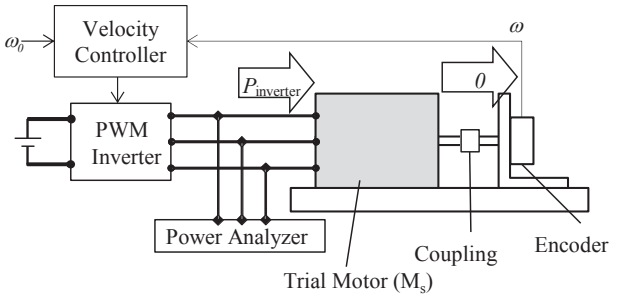

Fig. 7 Schematic diagram of the iron loss measurement system by no-load test.

3.3 Measurement Results of Drag Force Test

The IPMSM iron loss is measured at 750 rpm, 1500 rpm, 2250 rpm and 3000 rpm which correspond to an electrical fundamental frequency of 50 Hz, 100 Hz, 150 Hz and 200 Hz respectively. The results obtained for both IPMSMs (with GO stator and with NO stator) are shown in Fig. 8. The bars represent the standard deviation of the ten measurements. The iron loss reduction calculated considering the average of the ten measurements is also presented in Fig. 8. Even though the reduction could be considered small given the increased manufacture complexity, a reduction is observed and is considered to be due to the superior characteristics of GO steel [17] and the laser scratch that downsizes the magnetic domains and then reduce the excess loss [18].

3.4 Measurement Results of No-load Test

The iron losses measured under no-load operation are illustrated in Fig. 9. As in the previous section, the standard deviation of the ten measurements is also illustrated using bars. The PWM inverter causes high order harmonics in the magnets, rotor and stator magnetic flux that contribute to increase the iron loss compared to drag force operation [19)-20)]. Under PWM inverter excitation also, it appears that the GO stator decreases the IPMSM iron loss. However, the reduction percentage is smaller compared to the drag force condition, especially at 750 rpm (50 Hz). This can be explained by the fact that the GO material is originally intended for application at 50/60 Hz and has its best reduction potential at these frequencies compared to NO. At higher frequencies, the iron loss density reduction worsens, as shown by Table IV.

4. Analysis of Magnetic Anisotropic Motor

The measured iron loss data need to be confirmed by numerical calculation. Here, a 2-dimensional (2-D) model for magnetic field analysis and Steinmetz equations for iron loss calculation are used. Some assumptions and simplifications are made and detailed in the following sections, along with their possible consequences. It should be noted that the aim of this paper is to evaluate the potential gain of using GO steel in the proposed configuration and numerical analysis is done to confirm the experimental data. Since the final purpose of the paper is not to propose a novel numerical model, it is considered that the simplifications and assumptions could lead to possible inaccuracies but are acceptable given the targeted purpose.

4.1 Method for Magnetic Field Analysis

The 2-D model is based on FEA with A-method used as in ref. 21). The fundamental equation is expressed as follows:

$$\frac{\partial}{\partial x}\left(v_y \frac{\partial}{\partial x} A_z\right)+\frac{\partial}{\partial y}\left(v_x \frac{\partial}{\partial y} A_z\right) = -J_0+\sigma \frac{\partial}{\partial t} A_z - v_0 \frac{\partial}{\partial x} M_y + v_0 \frac{\partial}{\partial y} M_x \quad (4)$$

where A_z is the vector potential on the z-axis, v_x and v_y are the magnetic reluctivity on the x and y axis, v_0 is the space magnetic reluctivity, J_0 is the current density supplied to the coil parts, σ is the electrical conductivity of the material, and M is the magnetization of permanent magnets.

In the GO stator, two-axis anisotropic method is used to model the magnetic anisotropy. It provides satisfactory magnetic field analysis when the material is not magnetically saturated [22)]. The magnetic reluctivity v_x is the reluctivity of GO in the easy magnetization axis and v_y is the reluctivity in the transverse magnetization axis. They are calculated from Fig. 1.a. Since the easy axis and transverse axis direction change at each tooth and yoke part, it is impossible to take a unique (x, y) reference frame for the whole numerical model. Consequently, each tooth or yoke part has its own reference frame.

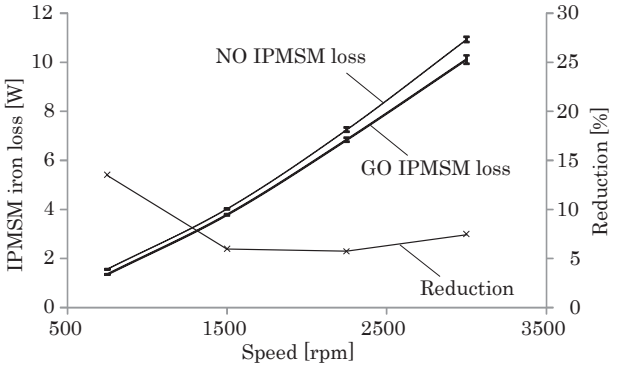

Fig. 8 Iron loss comparison between magnetic anisotropic motor and IPMSM with NO stator core under drag force operation.

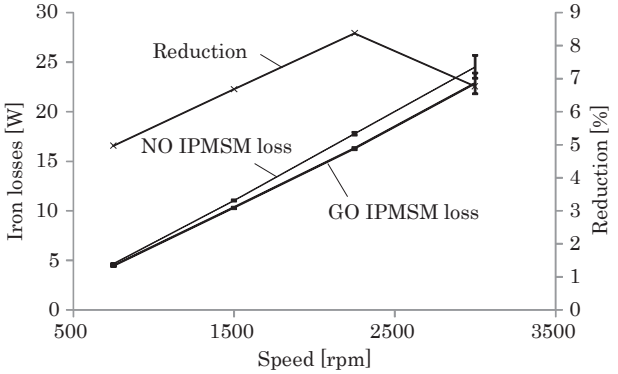

Fig. 9 Iron loss comparison between magnetic anisotropic motor and IPMSM with NO stator core under no-load operation.

TABLE IV MATERIAL IRON LOSS DENSITY OF NO (35H300) AND GO (35ZH135) AT B= 1 T.

Exciting frequency (Hz)	50	100	200	1000
NO (W/kg)	1.06	2.54	6.59	77.8
GO easy magnetization direction (W/kg)	0.415	1.25	3.90	64.1
Reduction ratio (%)	60.9	51.0	40.8	17.6

Similarly to the Epstein frame configuration explained in the introduction, the NO stator lamination is done by stacking the cut sheets with different orientation angles (made possible by the several symmetries of the stator shape). In this way, the stator has small local anisotropy but can be considered to have a global magnetic isotropy since the material orientation angle differs through the stator axial length, covering the whole angle range. As a consequence, it is possible to use a single average *B*-*H* characteristic in the FEA model without causing large inaccuracies. In other words, ν_x and ν_y are considered equal in (4) for the model of the NO stator.

Because of the interlamination insulation and the fact that a 2-D model is used, the electrical conductivity is taken null in the stator and rotor. The magnetic field induced by the eddy current is not considered and the eddy current losses are approximated by using the Steinmetz equations. The electrical conductivity of permanent magnets however is considered and the magnets eddy current losses are obtained from the calculation of the eddy currents flowing in the magnets. Moreover, the magnetic reluctivity of the magnets is taken equal to that of the air.

When simulating the drag force operation, J_0 is taken null since there is no current in the coils. When simulating the no-load operation, the phase current that has been measured during the no-load tests are used as input of the numerical model. In other words, the current density J_0 is calculated based on the measured phase current.

To evaluate the iron loss density W_{GO} in the GO stator, the magnetic flux density is first decomposed into its components in the easy magnetization direction B_e and the transverse magnetization direction B_h. In this way, the decomposition of the magnetic flux density vector depends on the part (yoke or tooth) that is considered. A fast Fourier transform (FFT) is then performed to find the harmonic components of B_e and B_h [23]. Finally, the iron loss density at each point is calculated using the Steinmetz approximation [24)-25)].

$$W_{GO} = \sum_{i=1}^{N} \{(K_{hys,e,i} B^2_{e,i} + K_{hys,h,i} B^2_{h,i}) f_i + (K_{ed,e,i} B^2_{e,i} + K_{ed,h,i} B^2_{h,i}) f^2_i\} \quad (5)$$

where i is the harmonic rank, N is the rank of the highest harmonic, f_i is the frequency of the i^{th} harmonic, and $B_{h,i}$ and $B_{e,i}$ are the amplitudes of the i^{th} harmonic of B_h and B_e respectively. $K_{hys,e,i}$ and $K_{hys,h,i}$ are the hysteresis loss Steinmetz constants of the GO in the easy and transverse magnetization directions respectively. $K_{ed,e,i}$ and $K_{ed,h,i}$ are the eddy current loss Steinmetz constants of the GO in the easy and transverse magnetization direction respectively.

As the NO stator is considered to have global magnetic isotropy, the following equation can be used instead of (5) for the calculation of the iron loss density.

$$W_{NO} = \sum_{i=1}^{N} \{K_{hys,i} (B^2_{t,i} + B^2_{r,i}) f_i + K_{ed,i} (B^2_{t,i} + B^2_{r,i}) f^2_i\} \quad (6)$$

where unlike (5), the magnetic flux density is decomposed into its radial B_r and tangential B_t components and the Steinmetz constants do not depend on the direction in the material as shown by the disappearance of the index h and e. The Steinmetz constants depend on the frequency as shown by the index i, and are calculated using the "two-frequencies method". This method, illustrated in Fig. 10, is basically an interpolation using the material iron loss characteristics of Fig. 11. Figure 10 illustrates the case of NO but the same procedure is applied to GO for both the easy and transverse magnetization directions. The interpolation is done by considering the two available nearest frequencies to the frequency f_i.

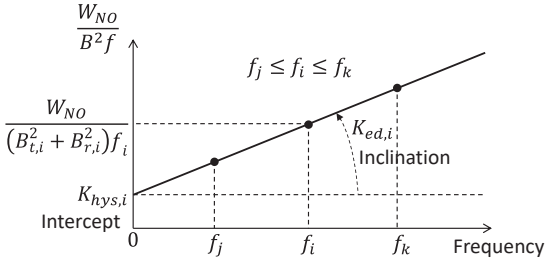

Fig. 10 Two-frequencies method to calculate the Steinmetz constants.

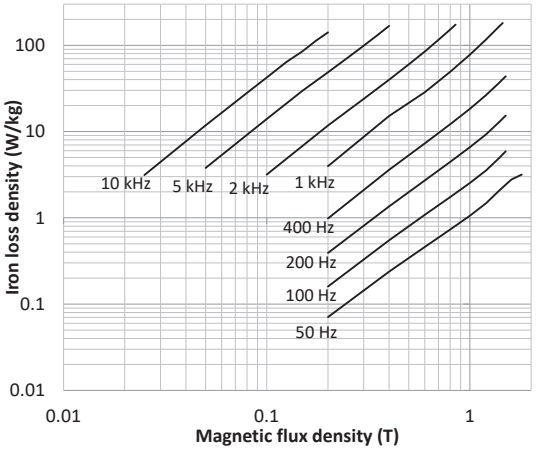

(a)

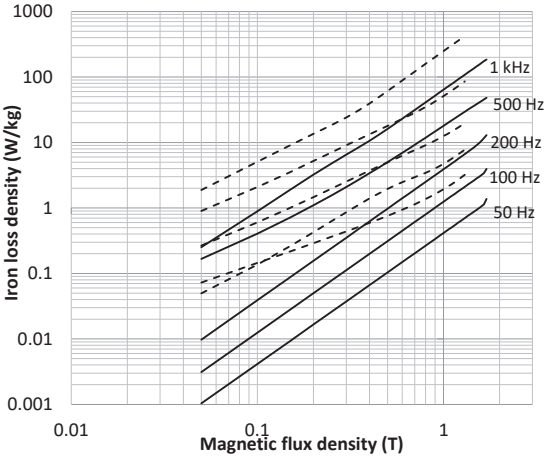

(b)

Fig. 11 Material iron loss density characteristics of GO and NO. (a) 35H300 (b) 35ZH135 easy magnetization direction (solid curve) and transverse direction (dashed curve).

Equations (5) and (6) are a sum through the harmonics of the magnetic flux density [26]. The harmonics in the stator magnetic flux caused by the rectangular magnets, the harmonics in the magnet and rotor magnetic flux caused by the stator slots, and the harmonics caused by the PWM inverter are taken into account in the calculation of the motor iron losses [27].

Moreover, even though the 2-D components of the magnetic flux density are considered in (5) and (6), the additional iron loss due to the rotation of the magnetic flux [28] is not modeled in this paper. For more accuracy, modeling the impact of rotational magnetic flux on the iron loss is preferable. However, for the NO material, previous works show that the approximation (6) results in a relatively good agreement between experiment and calculation [27),29]. As for the GO material, the permeability in the transverse direction is much lower than in the easy magnetization direction. Therefore, the question of whether or not the magnetic flux is rotating in the GO stator remains to be investigated at this stage. It is proposed to do this investigation for the case of drag force operation at 750 rpm. Through magnetic flux analysis, the magnetic flux density locus is calculated at three different points of the stator shown in Fig. 12. The magnetic flux density locus presents the variations of the components B_e and B_h of the magnetic flux density simultaneously through one electrical period. Fig. 13 shows the obtained results. It can be seen that for all points, the magnetic flux is stronger in the easy magnetization direction but the component in the transverse direction remains non-negligible, especially in the tooth part, showing that the magnetic flux is rotating. In order to confirm that, it is proposed to illustrate the magnetic flux lines at a given position of the rotor. The flux lines are shown in Fig. 14. It can be seen that some flux lines in the stator tooth are in the transverse direction especially when the tooth faces the space between two magnetic poles. Based on these observations, it is acknowledged that the impact of the rotational magnetic flux on the GO iron loss should be investigated in order to improve the model accuracy. Since it is a quite difficult task, this study is left for future work.

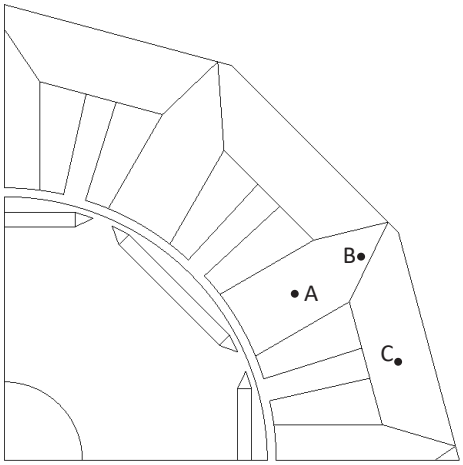

Fig. 12 Points considered for the investigation of the magnetic flux density locus.

Finally, the stator made of GO steel has much more cutting than the stator made of NO steel. It is known that cutting an electrical steel sheet increases the iron loss density in the vicinity of the cutting line. In this paper, wire electric discharge machining has been used for cutting. The paper does not aim at quantifying the impact of the cutting on the GO stator iron losses but it should be noted that wire electric discharge machining causes very low level damage and can even leave the material undamaged when the process is followed by stress relief annealing under nitrogen atmosphere at 820 °C for 3 hours [16]. It is then assumed that the damaged area will have only a small impact on the actual motor iron losses and consequently, the choice has been made not to model them in the FEA for a matter of simplification.

4.2 Influence of the Clearance Between the stator Pieces

The manufacture process of the GO stator results in a small clearance between the yoke and teeth pieces. The magnetic flux analysis results illustrated in the previous section is obtained using a finite element model that ignores the clearance.

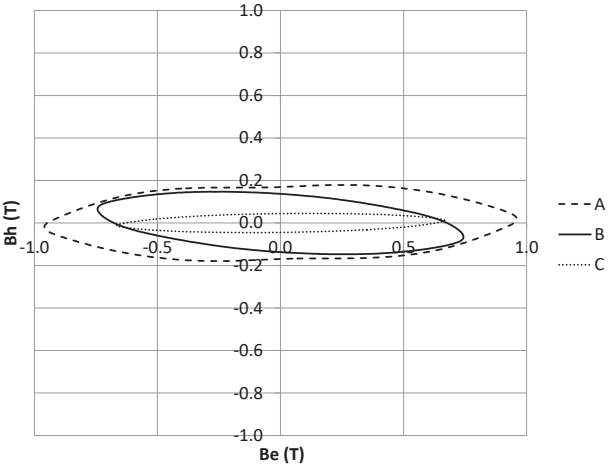

Fig. 13 Magnetic flux density locus in the GO stator obtained by FEA (drag force operation at 750 rpm).

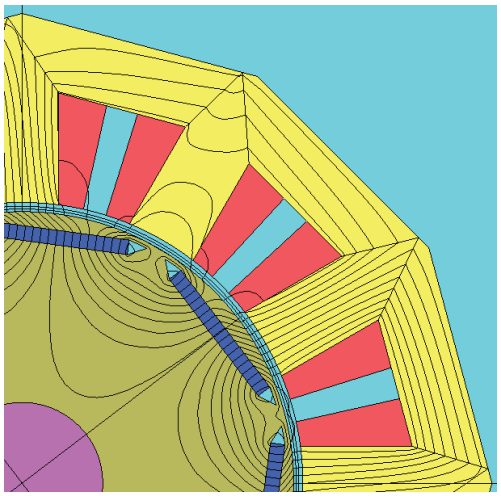

Fig. 14 Magnetic flux lines in the magnetic anisotropic motor (drag force operation at 750 rpm).

As a first approximation, it can be said that the total

reluctance of the magnetic flux path is mainly determined by the rotor/stator air gap plus the magnet and that the small clearance does not impact the total reluctance significantly. In this section it is proposed to evaluate the influence of the clearance on the stator magnetic flux density and iron losses.

If one considers a space factor of 98% in a laminated core of 350 µm thick steel sheets, it makes an interlamination of approximately 7 µm. The assembly of yoke and tooth parts has been done using an accurate jig [15] that ensures similar clearance between pieces while limiting mechanical pressure in the lamination direction. The clearance is then likely to be larger than 7 µm and slightly different at each junction. Choosing a representative clearance seems to be difficult but considering the above points, a model with a clearance of 10 µm is developed. Moreover, considering the tight clearance, unevenness due to imperfect cutting might locally affect the magnetic flux density. Because of the difficulty of modeling the unevenness of the air gap, the clearance has been chosen uniform through the whole gap in the new model.

The magnetic flux density locus obtained with the new model is illustrated in Fig. 15. The pieces clearance changes the magnetic flux density quite sensibly, especially in the T-joint part (point B), compared to the case in which there is no clearance (Fig. 13).

Table V gives the results of the IPMSM iron losses calculation using both models (with and without pieces clearance). Simulation results for both drag force and no-load operations at 750 rpm are presented. It can be seen that the iron losses are slightly lower when the clearance is included but the results remain close. Considering the above observations, it is decided to keep the model including pieces clearance for all the simulations whose results are presented in the next section.

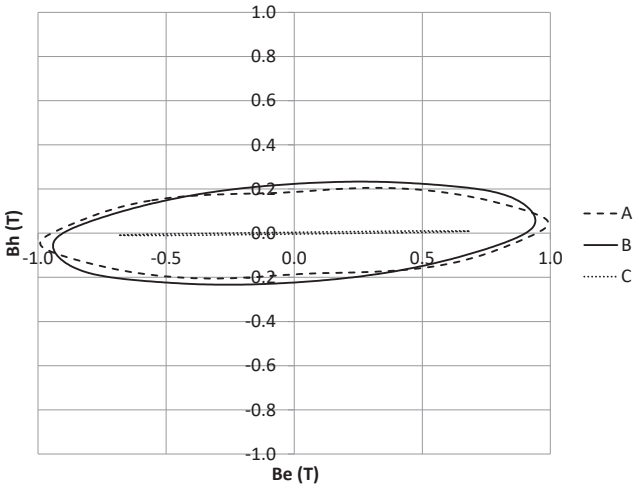

Fig. 15 Magnetic flux density locus in the GO stator obtained by FEA considering the pieces clearance (drag force operation at 750 rpm).

4.3 Calculation Results

Fig. 16 and Fig. 17 show the measurements and the numerical analysis results of both magnetic anisotropic and NO IPMSMs iron losses in drag force and no-load conditions respectively. For both numerical analysis and experiments, the magnetic anisotropic IPMSM has lower iron losses than the NO IPMSM.

TABLE V IRON LOSS CALCULATION RESULTS OBTAINED BY 1) MODEL CONSIDERING PIECES CLEARANCE, 2) MODEL WITHOUT PIECES CLEARANCE (750 RPM)

		No clearance [W]	With clearance [W]
Drag force	IPMSM total iron loss	1.53	1.49
	Stator loss	1.134	1.095
	Rotor loss	0.356	0.353
	Magnet loss	0.0408	0.0391
No-load	IPMSM total iron loss	2.86	2.81
	Stator loss	1.250	1.212
	Rotor loss	0.526	0.521
	Magnet loss	1.086	1.077

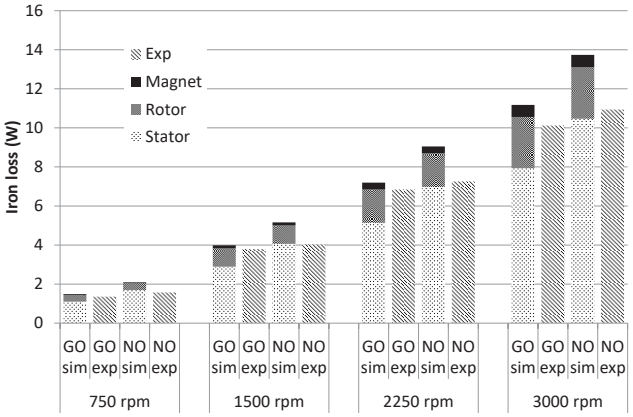

Fig. 16 Numerical analysis and measurements of IPMSM iron losses in drag force condition.

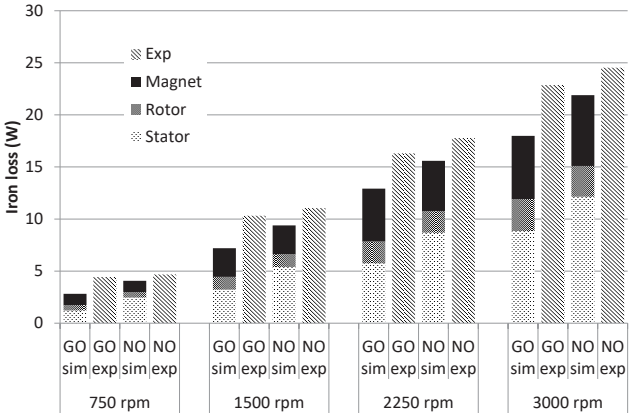

Fig. 17 Numerical analysis and measurements of IPMSM iron losses in no-load condition.

However, the iron loss difference between the magnetic anisotropic motor and the NO IPMSM is larger for the numerical calculation than for the experiments. In particular, at 3000 rpm for example, the measurements show a decrease of total iron losses by about 7.5 % in drag force condition and 6.8 % in no-load condition. In comparison for the same speed, FEA results show that the magnet and rotor iron losses are very similar for both motors but the stator iron losses drop by about 24 % in drag force operation and 27 % in no-load operation when the GO stator is used. As explained in section 4.1, the rotational losses have not been taken into account in the FEA neither for the NO IPMSM nor the magnetic anisotropic motor. It is thought that the rotational magnetic flux density in the GO material may have a bigger impact than for the NO material, which could explain the lower iron loss decrease obtained by experiment. Moreover, both experiment and numerical calculation show an increase of iron losses between the drag force and the no-load operations. This is due to the high frequency voltage supplied to the motor coils by the PWM inverter in no-load condition [19)-20)]. The magnet eddy currents are especially strongly affected [30)].

The peak magnetic flux density and the iron loss distributions calculated by FEA for drag force operation at 750 rpm are presented in Fig. 18 and Fig. 19 for the NO IPMSM and the magnetic anisotropic motor respectively. It should be noted that the iron loss distribution shows only the rotor and stator iron losses but not the magnet eddy current losses because both are made at different calculation steps. In the NO IPMSM the magnetic flux flows from the tooth to the yoke concentrated in the inner area and the magnetic

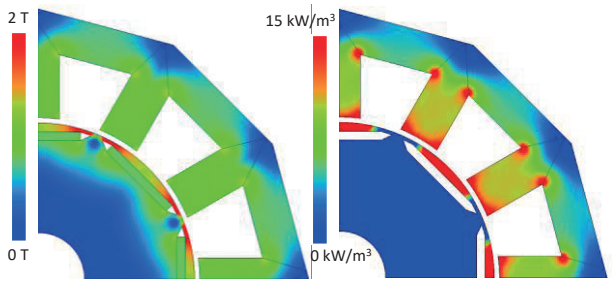

(a) Magnetic flux density (b) Iron loss density

Fig. 18 Peak magnetic flux density and iron loss density distributions of NO IPMSM at 750 rpm (drag force operation).

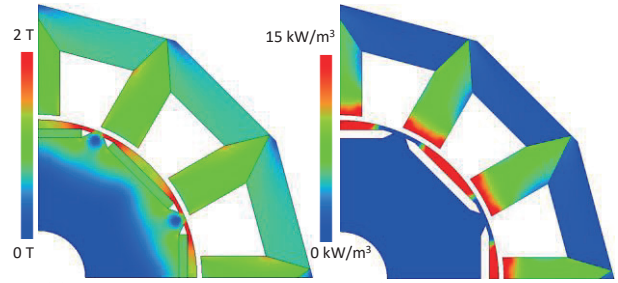

(a) Magnetic flux density (b) Iron loss density

Fig. 19 Peak magnetic flux density and iron loss density distributions of magnetic anisotropic motor at 750 rpm (drag force operation).

flux density in the outer of the tooth/yoke junction area remains low. Comparatively, for the magnetic anisotropic motor, the magnetic flux rotates less and remains as much as possible in the easy magnetization direction. Therefore it flows all the way towards the outer of the T-joint area, resulting in a higher iron loss density compared to the NO stator in this zone. Everywhere else, the iron loss density in the GO stator is smaller than in the NO stator. For both motors, the peak magnetic flux density in the tooth is higher than in the yoke, which results in higher iron loss density. The difference of iron loss density between the tooth and yoke parts seems to be more accentuated in the GO stator though. This can be explained by the fact that, besides the higher peak magnetic flux density, the magnetic flux density component in the transverse direction is larger in the tooth part than in the yoke part (Fig. 15).

5. Conclusion

A novel permanent magnet synchronous motor using a stator made of grain-oriented steel sheets has been evaluated. In drag force test conditions at 750 rpm, the experiments show that the iron losses of the proposed motor are 13.5 % lower than the iron losses of its equivalent motor using exclusively non-oriented silicon steel. The reduction becomes 5 % in no-load condition at 750 rpm.

The GO stator requires more cutting than a conventional stator and a low damage cutting technique is preferred knowing the sensitivity of GO to mechanical stress. Consequently, even though GO can reduce the motor iron losses, the GO stator manufacture is more costly, making it more suitable for special applications like aircrafts or spaceships at this moment. Moreover, numerical analysis could be improved by taking rotational losses and cutting damage into account. Finally, a simple geometry has been chosen for the stator core proposed in this paper. Thus, further optimization is still a possible future investigation in order to fully benefit from the characteristics of the GO material.

Acknowledgements This research is partially supported by KAKENHI (26420259) of Ministry of Education, Culture, Sports, Science and Technology.

References

1) K. Fujisaki: "Future Magnetic Material Property Installed in and Driven by Power Electronics Technology," *IUMRS-ICAM 2015 (14th Int. Union Materials Res. Soc. – Int. Conf. Adv. Materials)*, IV-1Th3F1-1 (IS), 2015.10.29.
2) N. P Goss: "Electrical sheet and method and apparatus for its manufacture and test," *U.S. Patent 1965559*, 1934.
3) S. Taguchi, T. Yamamoto, and A. Sakakura: "New grain-oriented silicon steel with high permeability "ORIENTCORE HI-B"," *IEEE Trans. on Magn.*, vol. **10**, pp. 123–127, 1974.
4) K. Honda, and S. Kaya: "On magnetization of single crystals of iron," *Sci. Rep. Tohoku Imp. Univ.*, vol. **15**, p. 721, 1926.

5) Nippon Steel Cat. No. SC 503 63.3, 1992.2.
6) S. Lopez, B. Cassoret, J. F. Brudny, L. Lefebvre, and J. N. Vincent: "Grain oriented steel assembly characterization for the development of high efficiency AC rotating electrical machines," *IEEE Trans. Magn.*, vol. **45**, no. 10, pp. 4161–4164, Oct. 2009.
7) S. Cicalé, L. Albini, F. Parasiliti, and M. Villani: "Design of a permanent magnet synchronous motor with grain oriented electrical steel for direct-drive elevators," in *Proc. XXth Int. Conf. Electrical Machines (ICEM)*, Marseille, 2012, pp. 1256–1263.
8) Y. Sugawara, and K. Akatsu: "Characteristics of a switched reluctance motor using grain-oriented electric steel sheet," in *Proc. Int. Conf. Electrical Machines and Systems (ICEMS)*, Busan, 2013, pp. 18–23.
9) Y. Enomoto, M. Kitamura, T. Sakai, and K. Ohara: "A way to select electrical sheets of the segment stator core motors," *IEEJ Trans. Ind. Appl.*, vol. **124**, no. 10, pp. 1010–1016, 2004. (in Japanese)
10) Y. Matsuo, T. Higuchi, T. Abe, Y. Miyamoto, and M. Ohto: "Characteristics of a novel segment type switched reluctance motor using grain-oriented electric steel," in *Proc. Int. Conf. Electrical Machines and Systems (ICEMS)*, Beijing, 2011, pp. 1–4.
11) S. Taghavi, and P. Pillay: "A novel grain-oriented lamination rotor core assembly for a synchronous reluctance traction motor with a reduced torque ripple algorithm," *IEEE Trans. Ind. Appl.*, vol. **52**, no. 5, pp. 3729-3738, Sep./Oct. 2016.
12) R. Koga, T. Todaka, and M. Enokizono: "Vector magnetic characteristic analysis of segment type synchronous reluctance motor utilizing grain-oriented electrical steel sheet," in *Proc. 15th Int. Conf. Electrical Machines and Systems (ICEMS)*, Sapporo, 2012, pp. 1–6.
13) J. Ma, R. Qu, and J. Li: "A novel axial flux switched reluctance motor with grain oriented electrical steel," in *Proc. IEEE Magn. Conf. (INTERMAG)*, Beijing, 2015, pp. 1-1.
14) K. Fujisaki, and K. Fujitani: "Design of stator core shape of 'magnetic anisotropic motor'," in *Proc. XXth Int. Conf. on Electrical Machines (ICEM)*, Marseille, 2012, pp. 183–189.
15) S. Takeda, K. Fujitani, S. Odawara, and K. Fujisaki: "Trial manufacture of magnetic anisotropic motor and evaluation of drag loss characteristics," in *Proc. Int. Conf. Electrical Machines (ICEM)*, Berlin, 2014, pp. 2055-2061.
16) H. Naumoski, B. Riedmüller, A. Minkow, and U. Herr: "Investigation of the influence of different cutting procedures on the global and local magnetic properties of non-oriented electrical steel," *J. of Magnetism and Magnetic Materials*, vol. **392**, pp. 126-133, Oct. 2015.
17) T. Kubota, M. Fujikura, M. Mizokami, and Y. Ushigami: "Electrical steel sheet for eco-design of electrical equipment," *Nippon Steel Technical Report*, no. 81, pp.53–57, Jan. 2000.
18) S. Aihara, H. Shimoji, T. Todaka, and M. Enokizono: "Measurement of local vector magnetic properties in laser scratched grain-oriented silicon steel sheet with vector-hysteresis sensor," *IEEE Trans. Magn.*, vol. **48**, no. 11, pp. 4499-4502, Nov. 2012.
19) A. Boglietti, P. Ferraris, M. Lazzari, and F. Profumo: "Iron losses in magnetic materials with six-step and PWM inverter supply [induction motors]," *IEEE Trans. Magn.*, vol. **27**, no. 6, pp.5334–5336, 1991.
20) N. Denis, K. Fujitani, Y. Kato, M. Ieki, and K. Fujisaki: "Core loss increase due to inverter carrier frequency in an interior permanent magnet synchronous motor," in *Proc. Int. Conf. Electrical Machines and Systems (ICEMS)*, Pattaya, 2015, pp. 1-7.
21) T. Nakata, and N. Takahashi: "Direct finite element analysis of flux and current distributions under specified conditions," *IEEE Trans. Magn.*, vol. **18**, no. 2, pp. 325-330, Mar 1982.
22) T. Tamaki, K. Fujisaki, K. Wajima, and K. Fujiwara: "Comparison of magnetic field analysis methods considering magnetic anisotropy," *IEEE Trans. Magn.,* vol. **46**, no.2, pp. 187–190, Feb. 2010.
23) L. Petrea, C. Demian, J. F. Brudny, and T. Belgrand: "High-frequency harmonic effects on low-frequency iron losses," *IEEE Trans. Magn.*, vol. **50**, pp. 1–4, Nov. 2014.
24) C. P. Steinmetz: "On the law of hysteresis," *Trans. Amer. Inst. Elec. Eng.*, vol. **IX**, no. 1, pp.1-64, Jan. 1892.
25) C. P. Steinmetz: "On the law of hysteresis (Part II.) and other phenomena of the magnetic circuit," *Trans. Amer. Inst. Elec. Eng.*, vol. **IX**, no. 1, pp. 619–758, Jan. 1892
26) K. Yamazaki, and H. Ishigami: "Rotor-shape optimization of interior-permanent-magnet motors to reduce harmonic iron losses," *IEEE Trans. Ind. Electro.*, vol. **57**, no. 1, pp. 61–69, Jan. 2010.
27) K. Yamazaki, and Y. Seto: "Iron loss analysis of interior permanent-magnet synchronous motors – variation of main loss factors due to driving condition," *IEEE Trans. Ind. Appl.*, vol. **42**, no. 4, pp. 1045–1052, Jul./Aug. 2006.
28) Y. Guo, J. G. Zhu, J. Zhong, H. Lu, and J. X. Jin: "Measurement and modeling of rotational core losses of soft magnetic materials used in electrical machines: A review," *IEEE Trans. on Magn.*, vol. **44**, no. 2, pp. 279-291, Feb. 2008.
29) S. Okamoto, N. Denis, Y. Kato, M. Ieki, and K. Fujisaki: "Core loss reduction of an interior permanent-magnet synchronous motor using amorphous stator core," *IEEE Trans. Ind. Appl.*, vol. **52**, no. 3, pp. 2261-2268, May/Jun. 2016.
30) K. Yamazaki, and A. Abe: "Loss investigation of interior permanent-magnet motors considering carrier harmonics and magnet eddy currents," *IEEE Trans. Ind. Appl.*, vol. **45**, no. 2, pp. 659-665, Mar./Apr. 2009.

Received Nov. 01, 2017; Accepted Mar. 27, 2018

J. Magn. Soc. Jpn., **42**, 72-77 (2018)

<Paper>

Magnetostrictive Behaviors of fcc-Co(001) Single-Crystal Films Under Rotating Magnetic Fields

Tetsuroh Kawai[1], Mitsuru Ohtake[1, 2], and Masaaki Futamoto[1]

[1]Faculty of Science and Engineering, Chuo University, *1-13-27 Kasuga, Bunkyo-ku, Tokyo 112-8551, Japan*

[2]Faculty of Engineering, Kogakuin University, *2665-1 Nakano, Hachiohji, Tokyo 192-0015, Japan*

Magnetostrictive behaviors of fcc-Co(001) single-crystal films with thicknesses ranging from 40 to 500 nm are investigated under rotating magnetic fields up to 1.2 kOe. The magnetocrystalline anisotropy estimated from the magnetization curves is confirmed to be lying with four-fold symmetry, and the anisotropy field is within a narrow range of 900~950 Oe for these films. The easy and the hard axes are lying parallel to <110> and <100>, respectively. The magnetostrictive behavior measured along [110] shows rectangular or bathtub-like waveform and the amplitude does not change much when the magnetic field is increased. On the contrary, the behavior along [100] shows triangular waveform and the amplitude increases with increasing the magnetic field. These characteristic behaviors are explained by using a coherent rotation model of magnetization assuming an in-plane four-fold magnetic anisotropy. The magnetostriction constants (λ_{100}, λ_{111}) estimated from the amplitudes measured at 1.2 kOe are λ_{100}=(85~90)×10^{-6} and λ_{111}=−(40~50)×10^{-6}, respectively for these films. The λ_{100} values are in agreement with that estimated by the first-principle calculation.

Key words: fcc-Co, magnetocrystalline anisotropy, magnetostriction, single-crystal film

1. Introduction

The crystal structure of Co metal is known to be hexagonal close packed (hcp) at room temperature and it changes to face centered cubic (fcc) over 450°C according to the phase diagram. On the other hand, meta-stable fcc-Co appears even at room temperature in the films prepared by molecular beam epitaxy or spattering process [1-4]. Single-crystal films of fcc-Co(001) are prepared by hetero-epitaxial film growth on Cu(001) underlayers, and their magnetic anisotropies are reported to be with the easy and the hard axes along <110> and <100>, respectively [5-7]. Magnetic properties of fcc-Co are different from those of hcp-Co [7, 8]. However, systematic magnetostriction studies of fcc-Co(001) single-crystal films have not yet been reported.

In the present study, well defined fcc-Co(001) single-crystal films are prepared on MgO(001) single-crystal substrates by employing Pd and Cu underlayers and the magnetostrictive behaviors are investigated under rotating magnetic fields up to 1.2 kOe. The experimental results are analyzed by using a coherent rotation model of magnetization considering the magnetocrystalline anisotropy.

2. Experimental Procedure

Co films with thicknesses of 40~500 nm were prepared on MgO(001) single-crystal substrates of 20×20×0.5 mm^3 with Pd (10 nm) and Cu (10 nm) underlayers at 300 °C by using a radio-frequency magnetron sputtering system equipped with a reflection high energy electron diffraction (RHEED) facility. The base pressures were lower than 4×10^{-7} Pa. Before film formation, the MgO substrates were heated at 600 °C for 1 hour in the ultra-high vacuum chamber to obtain clean surface, which was confirmed by RHEED. The underlayers of Pd and Cu were employed to adjust the lattice mismatch (16%) between MgO and fcc-Co and also to promote Co thin film growth with a metastable fcc structure [4]. The film structure was confirmed by RHEED and X-ray diffraction (XRD) with Cu-Kα radiation (λ=0.15418 nm). Magnetization curves were measured by using a vibrating sample magnetometer (VSM). Magnetostriction measurements were carried out by using a cantilever method under rotating magnetic fields up to 1.2 kOe [9]. The rotating speed was 5 rpm. The magnetostriction observation directions were set along [100] and [110] of the MgO(001) substrates. The magnetostriction coefficient λ is calculated from the following formula [9].

$$\lambda = \frac{\Delta S \cdot t_s^{\,2}}{3L^2 \cdot t_f} \cdot \frac{E_s \cdot (1+\nu_f)}{E_f \cdot (1-\nu_s)}, \qquad (1)$$

where ΔS is the measured bending, L is the distance between laser beam points (12.5 mm), t is the thickness, E is Young's modulus, ν is Poisson's ratio, and the subscripts of f and s respectively refer to film and substrate. For the single-crystal films and the single-crystal substrates, the values shown in Table 1 are employed because the elastic property of single-crystal sample is anisotropic[10]. In the calculations, the elastic stiffness values of fcc-Ni were employed for the values of fcc-Co because the stiffness values of fcc-Co were unknown [11].

Table 1 E and ν values of fcc-Co and MgO materials used in the present study [10, 11].

	fcc-Co		MgO	
Orientation	<100>	<110>	<100>	<110>
E [GPa]	129	227	185	215
ν	0.384	−0.085	0.34	0.23

3. Results and Discussion

3.1 Crystal structure of Co films grown on Cu/Pd underlayers

RHEED patterns observed for Co films grown on Cu/Pd underlayers are shown in Fig. 1. Similar sharp streaks are observed for the Co films of different thicknesses ranging from 40 to 500 nm, which indicates that the films are single-crystals with smooth surfaces.

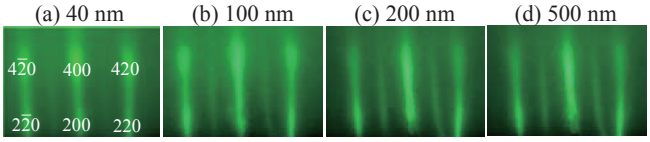

Fig. 1 RHEED patterns observed for Co films of (a) 40, (b) 100, (c) 200, and (d) 500 nm thicknesses. The incident electron beam is parallel to MgO[100].

Figure 2 shows the out-of-plane and the in-plane XRD patterns observed for these Co films. The fcc(002) and (004) peaks are clearly recognized in addition to the reflections from the MgO substrates and the Cu/Pd underlayers. Therefore, the films are determined to be fcc(001) single-crystal films. The epitaxial orientation relationship to the MgO substrate is determined as

fcc-Co(001)[100] ∥ MgO(001)[100].

The lattice parameters determined from the peak positions of fcc(002) in the out-of-plane and the in-plane XRDs are shown in Fig. 3. The lattice parameter measured parallel to the substrate surface, a, is larger than that measured perpendicular, c, for the thickness range between 40 and 500 nm, indicating that the fcc-crystal is slightly deformed. This is due to the hetero-epitaxial growth of fcc-Co(001) film on the fcc-Cu(001) under layer, where the lattice parameters of fcc-Cu (a=0.3614 nm) is 2.1% larger than that of bulk fcc-Co (a=0.354 nm) and the fcc-Co lattice is expanded in lateral direction. The difference of lattice parameters of fcc-Co(001) film decreases with increasing the film thickness as shown in Fig. 3 suggesting that the influence on the lattice strain from the Cu underlayer is decreasing with increasing the Co film thickness. The full width at half-maximum of rocking curves ($\Delta\theta_{50}$) is shown in Fig. 4 as a function of film thickness. The $\Delta\theta_{50}$ values measured from the out-of-plane and the in-plane XRDs are decreasing with increasing the film thickness, which indicate that the crystallographic quality is improved for thicker fcc-Co(001) films. These experimental results confirm that the Co films prepared

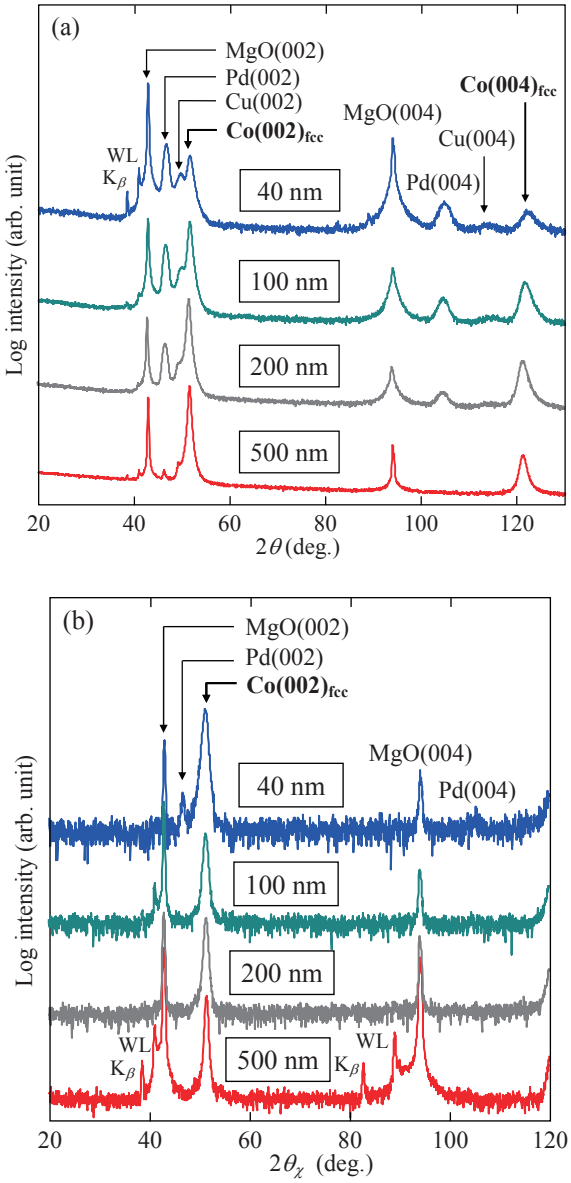

Fig. 2 XRD patterns observed for (a) out-of-plane and (b) in-plane of Co/Cu/Pd films formed on MgO(001) substrates. The Co film thickness is 40, 100, 200, and 500 nm, respectively.

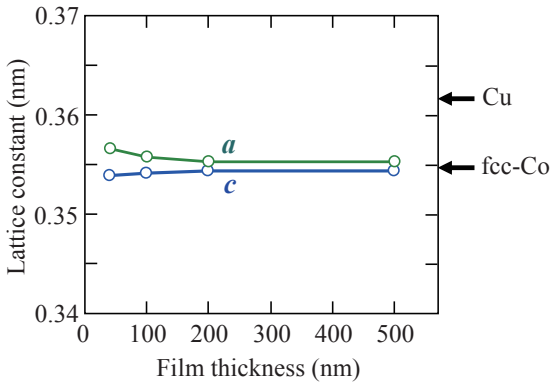

Fig. 3 Lattice constants determined from the fcc(002) peaks in the out-of-plane XRDs (c) and the in-plane XRDs (a) of Co films. Arrows show the lattice constants of bulk materials of Cu and fcc-Co.

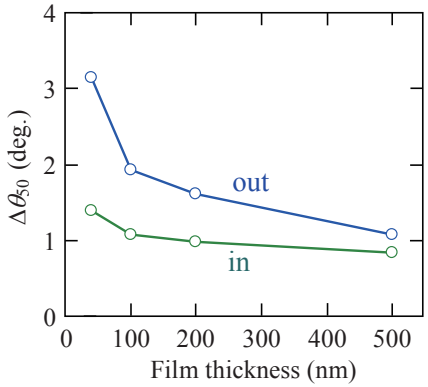

Fig. 4 Film thickness dependence of full width at half maximum of rocking curve ($\Delta\theta_{50}$) observed for the out-of-plane (out) and the in-plane (in) XRDs of Co films.

in the present study are single-crystal films with fcc(001) orientation involving very small lattice deformation which decreases with increasing the film thickness.

3.2 Magnetization curves of fcc Co(001) films

The magnetization curves of fcc Co(001) films measured with the magnetic field aligned parallel to [100] and [110] are shown in Fig. 5. All the films are showing similar types of M-H curve with the easy and the hard axes parallel to [110] and [100], respectively. The anisotropy filed matches to the saturation field for the cubic (001) film with four-fold anisotropy [12]. The anisotropy field (H_a) is estimated to be ranging from 900 to 950 Oe for the film thickness between 40 and 500 nm. The anisotropy field is nearly equal to those reported in the references [5-7]. The coercivities of these films are ranging between 40 and 50 Oe, which are far smaller than the H_a values (900-950 Oe). Such kind of magnetization curves can be expressed by using the modified coherent rotation model [12]. However, the detail of magnetization curve is slightly different depending on the film thickness. The M-H curves along

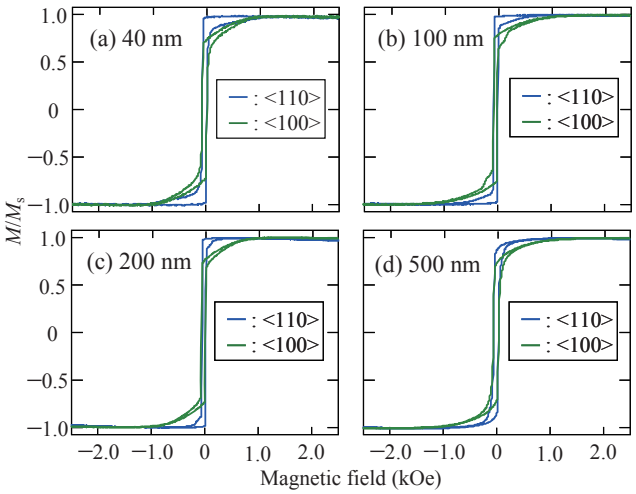

Fig. 5 Magnetization curves measured for fcc-Co(001) films with the thickness of (a) 40, (b) 100, (c) 200, and (d) 500 nm, respectively.

<110> for the (40-200) nm thick films show sharp shoulder, which means that the coherent rotation of magnetization is dominant in the magnetization process. On the other hand, the M-H curve for the 500 nm thick film shows mild shoulder, which means that the coherent rotation mode is slightly disturbed in the film. The small coercivities mean that the magnetic domain wall motions are dominant in the magnetization reverse process under small magnetic fields less than 50 Oe.

3.3 Magnetostrictive behavior of fcc-Co(001) films

Figure 6 shows the magnetostrictive behaviors measured along fcc[110] and [100] for the 40 nm thick film under rotating magnetic fields. The output voltage of 1 V corresponds to 0.2 μm bending of the sample. The rotating angle, 0, corresponds to [010] for λ//[110] and to [110] for λ//[100]. The output voltages are quite small,

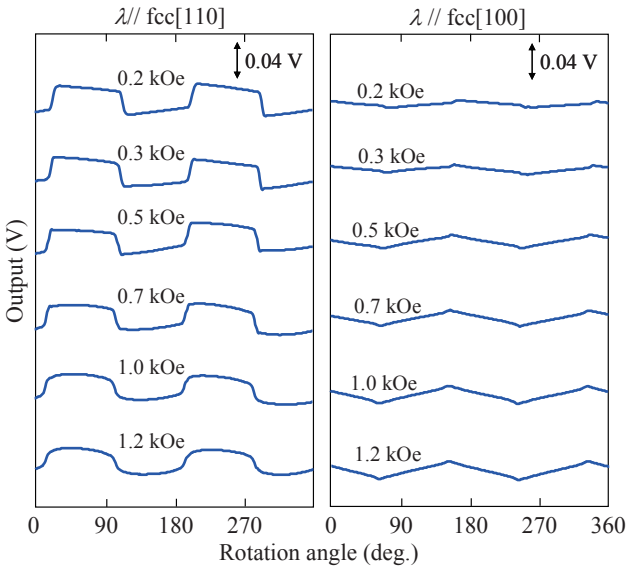

Fig. 6 Measured magnetostrictive behaviors of 40 nm thick fcc-Co(001) single-crystal film under rotating magnetic fields. The magnetostriction observation direction is along fcc[110] and [100], respectively.

since the film thickness is very small (40 nm) in comparison to that of MgO base substrate (0.5 mm), whereas the S/N ratio is good. The waveform along [110], namely along the easy magnetization axis, is rectangular under small magnetic fields up to 0.3 kOe and changes to bath-tub like with increasing the magnetic field, while the amplitude is kept at almost a similar level in the investigated magnetic field range. However, the waveform along [100], namely along the hard magnetization axis, is triangular in the investigated magnetic field range and the amplitude increase with increasing the magnetic field up to 1 kOe. The waveforms are different from ideal sinusoidal even under a high magnetic field of 1.2 kOe, which is larger than the magnetic anisotropy field. The output phase with respect to the magnetic field angle is opposite when measured along [110] and [100] directions, which

means that the sign of magnetostriction constant is opposite between the two orientations.

Figure 7 shows the magnetostrictive behaviors measured for the 100 nm thick film. The output amplitude is increasing in proportional to the film thickness. The waveforms measured along [110] and [100] resemble to those for the 40 nm thick film, namely the output waveform changes from rectangular to bath-tub like with increasing the magnetic field and the output intensity is kept almost at a similar amplitude along [110], whereas the output waveform measured along [100] is triangular and the amplitude increases with increasing the magnetic field.

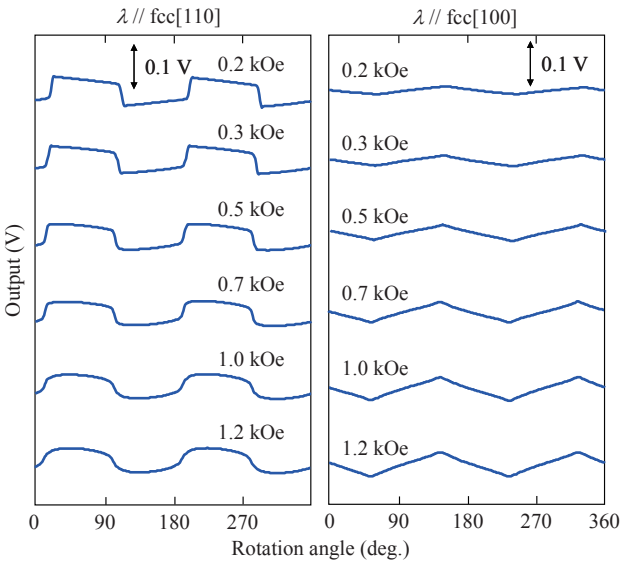

Fig. 7 Measured magnetostrictive behaviors of 100 nm thick fcc-Co(001) single-crystal film under rotating magnetic fields. The magnetostriction observation direction is along fcc[110] and fcc[100], respectively.

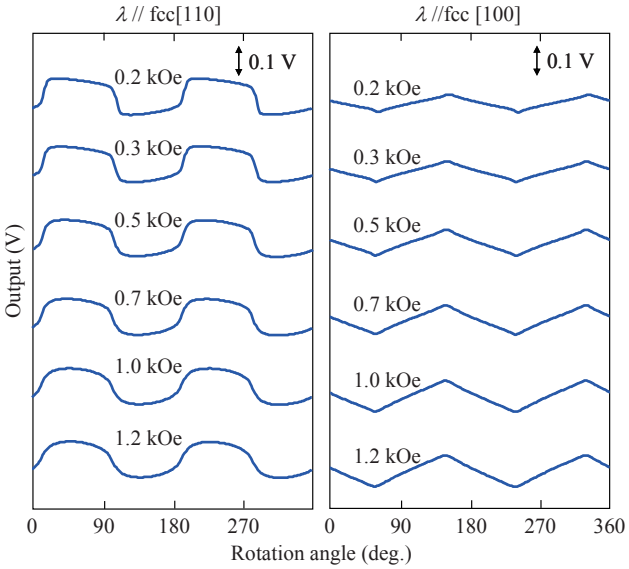

Fig. 8 Measured magnetostrictive behaviors of 200 nm thick fcc-Co(001) single-crystal film under rotating magnetic fields. The magnetostriction observation direction is along fcc[110] and fcc[100], respectively.

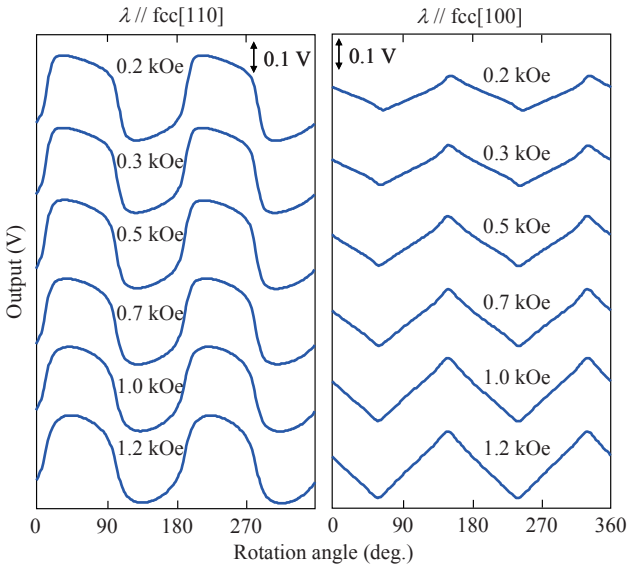

Fig. 9 Measured magnetostrictive behaviors of 500 nm thick fcc-Co(001) single-crystal film under rotating magnetic fields. The magnetostriction observation direction is along fcc[110] and fcc[100], respectively.

The output phases are reversed similar to the case of 40 nm thick film (Fig, 6). The waveforms for the 200 nm thick film shown in Fig. 8 are also similar to those for the 100 nm thick film. However, the waveforms for the 500 nm thick film are slightly different from those for 40 or 100 nm thick films. The waveform along [110] is not rectangular but bath-tub like even under a small magnetic field of 0.2 kOe. In the case that the magnetization process is based on a coherent rotation mode, the waveform should be rectangular under a sufficiently small magnetic field compared with its anisotropy field as reported in the previous report [13]. It is notable that the films with sharp rectangular M-H curves (Fig. 5), which are of the 40 and 100 nm thick films, show rectangular waveforms and the film with mild square M-H curve measured for the 500 nm thick film (Fig. 5) shows a bath-tub like waveform even under a small magnetic field. Therefore, the behavior of 500 nm thick film suggests that the magnetization process is deviating slightly from the coherent mode.

These unique magnetostrictive behaviors can be explained by considering coherent rotation of magnetization under a rotating magnetic field with taking into account the magnetocrystalline anisotropy[12, 13]. In the case that the intensity of rotating magnetic field is comparable to the magnetocrystalline anisotropy field, the magnetization tends to keep its direction parallel to the easy magnetization axis and tends to leave its direction from the hard magnetization axis. Only in the case where the intensity of rotating magnetic field is strong enough to overcome the anisotropy field, the magnetization will rotate under an influence of the applied rotating magnetic field and the magnetostrictive waveform is expected to be sinusoidal.

These behaviors are similar to those for bcc(001) single-crystal films with four-fold magnetocrystalline anisotropy [12, 13].

A phenomenological model is described as follows. The change in length by magnetostriction is given by the following equation for a cubic crystal [14].

$$\frac{\delta l}{l}=\frac{3}{2}\cdot\lambda_{100}\cdot\left(\alpha_1^2\cdot\beta_1^2+\alpha_2^2\cdot\beta_2^2+\alpha_3^2\cdot\beta_3^2-\frac{1}{3}\right)+3\cdot\lambda_{111}\cdot\left(\alpha_1\cdot\alpha_2\cdot\beta_1\cdot\beta_2+\alpha_2\cdot\alpha_3\cdot\beta_2\cdot\beta_3+\alpha_3\cdot\alpha_1\cdot\beta_3\cdot\beta_1\right) \quad (2)$$

Here λ_{100} and λ_{111} are the longitudinal magnetostriction for [100] and [111] directions, α's are the direction cosines of the magnetization with respect to the crystal axes, and βs the direction cosines of the measured length change. Since the change in length is a function of direction cosine of magnetization in this equation, it is based on a coherent rotation model. In a coherent rotation model, the free energy is given by the following equation considering magnetocrystalline anisotropy energy (K_1) and Zeeman energy ($M_s \cdot H_{ex}$).

$$E=\frac{1}{8}\cdot K_1\cdot\left(1-\cos 4\theta\right)+M_S\cdot H_{ex}\cdot\cos\left(\varphi-\theta\right) \quad (3)$$

Here θ and φ are the direction of M_s and H_{ex} with respect to the [100] axis in the (001) plane, respectively. For an observation direction of the change in length along [110] in the (001) plane, the equation (2) is rewritten as the following equation.

$$\frac{\delta l}{l}=\frac{1}{4}\cdot\lambda_{100}+\frac{3}{4}\cdot\lambda_{111}\cdot\sin 2\theta \quad (4)$$

This equation shows that the direction depending part depends only on λ_{111}, namely λ_{111} can be estimated from the measured amplitude along [110]. The magnetostrictive behavior along [100] can also be calculated. In this case, the equation (2) is rewritten as the following equation.

$$\frac{\delta l}{l}=\frac{1}{4}\cdot\lambda_{100}\cdot\left(1+3\cos 2\theta\right) \quad (5)$$

In the case, the direction depending part of the change in length depends only on λ_{100}, namely λ_{100} can be estimated from the measured amplitude along [100].

In order to calculate the change in length, we need to know the angle θ under an applied rotating magnetic field. The angle θ is determined so as to minimize the free energy, E in the equation (3). The calculated results are shown in Fig. 10 for h=1 and 2, where h is defined as $h=H_{ex}/H_a$. Therefore, the calculated results for h=1 are corresponding to the experimental results under H_{ex}=1.0 kOe and can explain the characteristic waveforms such as bath-tub like or triangular. The magnetostriction constants, λ_{100} and λ_{111} can be estimated from the amplitudes of output. Fig. 11 shows the output amplitude as a function of applied magnetic field up to 1.2 kOe. The amplitude along [110] keeps almost a same level and is well saturated in the

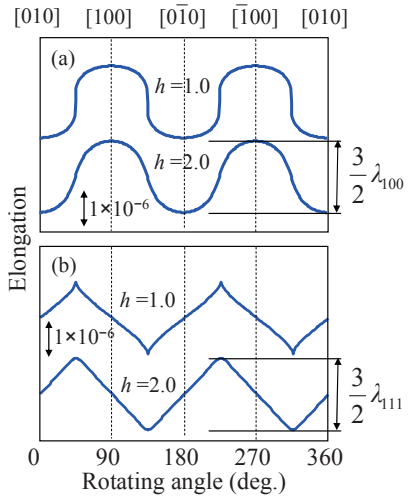

Fig. 10 Calculated magnetostrictive behaviors along (a) [110] and (b) [100]. λ_{100} and λ_{111} are assumed to be 10×10^{-6}. K_1 is assumed to be negative. h is defined as $h=H_{ex}/H_a$, where H_a is anisotropy field.

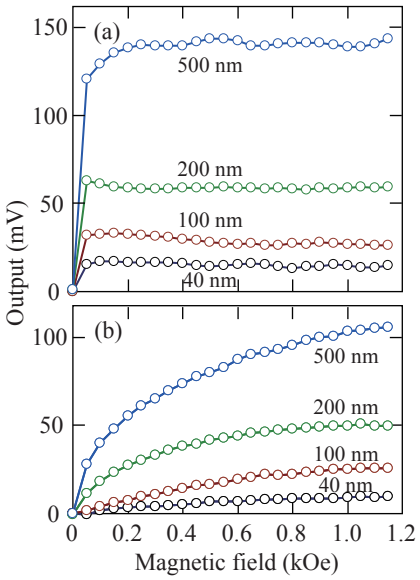

Fig. 11 Magnetic field dependence of output amplitude measured along (a) [110] and [100] of fcc-Co(001) single-crystal film sample with the thickness of 50, 100 200, and 500 nm, respectively.

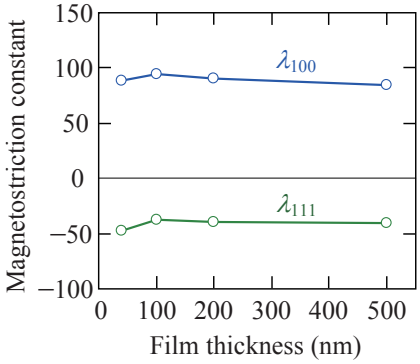

Fig. 12 Film thickness dependences of magnetostriction constants λ_{100} and λ_{111} estimated for fcc-Co(001) single-crystal films.

magnetic field range. However, the amplitude along [100] increases with increasing the magnetic field and the amplitudes for 40 nm, 100 nm, and 200 nm thick films are almost saturated at 1 kOe but that for 500 nm thick film is still approaching to saturation at 1.2 kOe. The estimated magnetostriction constants are shown in Fig. 12. The λ_{100} shows large positive value ranging from 85 to 90×10^{-6} and shows small film thickness dependence. The λ_{111} shows negative value ranging from -40 to -45×10^{-6} and also shows small film thickness dependence. The large positive value is consistent to the value calculated by a first principle method [15].

4. Conclusion

The magnetostrictive behaviors of fcc-Co(001) single-crystal films are investigated under rotating magnetic fields. The magnetostrictive behaviors along fcc[110] show rectangular or bath-tub like waveform and the amplitude is kept at almost a similar level, while the behaviors along fcc[100] show triangular and the amplitude increases with increasing the magnetic field. The behaviors can be explained by the coherent rotation model of magnetization assuming a four-fold magnetocrystalline anisotropy in (001) plain. The magnetostriction constant λ_{100} is determined to be large positive ranging from 85 to 90×10^{-6}, which agrees with that obtained by theoretical calculation. λ_{111} is negative ranging from -40 to -45×10^{-6}. The thickness dependences of λ_{100} and λ_{111} are confirmed to be very small for the fcc-Co(001) films.

Acknowledgements The authors would like to thank Prof. N. Inaba of Yamagata University for supporting the VSM measurements.

References

1) C. M. Schneider, P. Bressler, P. Schuster, and J. Kirschner: *Phys. Rev. Lett.* **64**, 1059 (1990).
2) B. Heinrich, J. F. CVochran, M. Kowalewski, J. Kirscher, Z. Celinski, A. S. Arrot, and K. Myrtle: *Phys. Rev.* B, **44**, 9348 (1991).
3) G. R. Harp, R. F. C. Farrow, D. Weller, T. A. Rabedeau, and R. F. Marks: *Phys. Rev. B*, **48**, 17538 (1993).
4) M. Ohtake, O. Yabuhara, J. Higuchi, and M. Futamoto: *J. Appl. Phys.*, **109**, 07C105 (2011).
5) P. Krams, F. Lauks, R. L. Stamps, B. Hillebrands, and G. Guntherodt: *Phys. Rev. Lett.* **69**, 3674 (1992).
6) D. Weller, G. R. Harp, R. F. C. Farrow, A. Cebollada, and J. Sticht: *Phys. Rev. Lett.* **13**, 2097 (1994).
7) T. Suzuki, D. Weller, C.-A. Chang, R. Savoy, T. Huang, B. A. Gurney, and V. Speriosu: *Appl. Phys. Lett.* **64**, 2736 (1994).
8) M. Takahashi and T. Miyazaki: Proc. 5th ICMTF (April 1972 at Mt. Fuji Area, Japan) B2-1 (1972).
9) T. Kawai, M. Ohtake, and M. Futamoto: *Thin Solid Films*, **519**, 8429 (2011).
10) T. Kawai, T. Aida, M. Ohtake, and M. Futamoto: *IEEE Trans. Mag.* **51**, 2007004 (2015).
11) C. Kittel: Introduction to Solid State Physics 8th edition, Chapter 3, p. 78 (John Wiley & Sons Inc., 2005).
12) T. Kawai, T. Aida, M. Ohtake, and M. Futamoto: *J. Magn. Soc. Jpn.,* **39**, 181 (2015).
13) T. Kawai, T. Aida, M. Ohtake, and M. Futamoto: *IEEE Trans. Mag.* **50**, 2008004 (2014).
14) S. Chikazumi: Physics of Ferromagnetism, p.121 (Syokabo, Tokyo, 1961).
15) R. Q. Wu, L. J. Chen, A. Shick, and A. J. Freeman: *J. Magn. Magn. Mater.* **177-181**, 1216 (1998).

Received Mar. 23, 2017; Accepted Feb. 22, 2018

J. Magn. Soc. Jpn., **42**, 78-82 (2018)

<Paper>

Magnetostriction Behaviors of Single- and Poly-Crystalline Ni/Ni-Co Bi-Layer Films

Kana Serizawa[1,2], Mitsuru Ohtake[1], Tetsuroh Kawai[1,2], Masaaki Futamoto[2], Fumiyoshi Kirino[3], and Nobuyuki Inaba[4]

[1]Faculty of Engineering, Yokohama National University, *79-5 Tokiwadai, Hodogaya, Yokohama 240-8501, Japan*

[2]Faculty of Science and Engineering, Chuo University, *1-13-27 Kasuga, Bunkyo-ku, Tokyo 112-8551, Japan*

[3]Graduate School of Fine Arts, Tokyo University of the Arts, *12-8 Ueno-koen, Taito-ku, Tokyo 110-8714, Japan*

[4]Faculty of Engineering, Yamagata University, *4-3-16 Jyonan, Yonezawa, Yamagata 992-8510, Japan*

Ni(t_{Ni} nm)/$Ni_{50}Co_{50}$(100–t_{Ni} nm) bi-layer films are prepared on Cu/Pd/MgO(001) single-crystal substrates at 300 °C and on Cu/Pd/glass substrates at room temperature by varying the layer thickness, t_{Ni}, in a range of 0–100 nm. The effect of layer thickness ratio on the magnetostriction is investigated. As t_{Ni} value increases from 0 to 100 nm, the magnetostriction coefficient observed for single-crystal film along fcc[100], λ_{100}, monotonically decreases from a positive value of $+1 \times 10^{-4}$ (t_{Ni} = 0 nm) to a negative value of -6×10^{-5} (t_{Ni} = 100 nm), whereas that measured along fcc[111], λ_{111}, remains almost similar (-4×10^{-5} to -2×10^{-5}). The magnetostriction coefficient of poly-crystalline film decreases from -3×10^{-6} to -2×10^{-5} with increasing t_{Ni} value from 0 to 100 nm. The present study has shown that control of magnetostriction coefficient is possible by combining materials with positive and negative coefficients.

Key words: Ni, Ni-Co alloy, thin film, magnetostriction coefficient, λ_{100}, λ_{111}

1. Introduction

Soft magnetic materials have been used for applications to magnetic devices, transformers, etc. In order to improve the performance, it is required to reduce the magnetostriction that causes vibration and is one of the origins for energy loss.

Ni-based alloys with fcc structure such as Ni-Fe and Ni-Co are typical soft magnetic materials. In the Ni-Co binary alloy system, fcc structure can be stabilized in the full compositional range through hetero-epitaxial thin film growth on Cu underlayer[1–3]. In our previous study[3], $Ni_{100-x}Co_x$ single-crystal films of fcc(001) orientation were prepared on Cu(001) underlayers by varying Co content, x, from 0 to 100 at. %. The magnetostriction coefficient of λ_{100} increased from a negative value of -3×10^{-5} to a large positive value of $+1 \times 10^{-4}$ with increasing Co content, whereas that of λ_{111} stayed almost constant around -2×10^{-5}. The compositional dependences were similar to the case of bulk Ni-Co alloy system[4].

Magnetostriction seems to be reduced by combining materials with negative and positive magnetostriction coefficients. In the present study, single- and poly-crystalline Ni/$Ni_{50}Co_{50}$ bi-layer films are prepared by varying the layer thicknesses while keeping the total thickness at 100 nm. The effect of layer thickness ratio on the magnetostriction coefficient is investigated.

2. Experimental Procedure

2.1 Film preparation

A radio-frequency magnetron sputtering system equipped with a reflection high-energy electron diffraction (RHEED) facility was used for film formation. Single- and poly-crystalline films were respectively prepared on MgO(001) single-crystal substrates of 0.3 mm thickness at 300 °C and on glass substrates of 0.14 mm thickness at room temperature. 5-nm-thick Pd buffer layers and 10-nm-thick Cu underlayers were sequentially deposited on the substrates. Then, Ni(t_{Ni} nm)/$Ni_{50}Co_{50}$(100–t_{Ni} nm) bi-layer films were formed on the underlayers. The Ni and the $Ni_{50}Co_{50}$ layer thicknesses were varied from 0 to 100 nm. The total bi-layer film thickness was fixed at 100 nm to obtain enough bending to detect by using our magnetostriction measurement system. The sputter deposition condition was similar to the case of our previous work[3].

The crystal structure and the crystallographic orientation were determined by RHEED. The resulting film structure was investigated by X-ray diffraction (XRD) with Cu-Kα radiation (wave length: 0.15418 nm). The magnetization curves were measured by vibrating sample magnetometry.

2.2 Magnetostriction measurement

Magnetostriction was measured by employing a laser displacement meter fixed on a vibration isolated table to measure the small cantilever bending with an accuracy of 1 nm. The output sensitivity was 1 V per 0.2 μm bending. A rotating magnetic field of 1.2 kOe was applied in the film plane. The rotating speed was 5 rpm.

Magnetostriction coefficient, λ, is expressed[5,6] as

$$\lambda = \{\Delta S\, t_s^2\, E_s\, (1 + \upsilon_f)\} / \{3\, L^2\, t_f\, E_f\, (1 - \upsilon_s)\}\,, \qquad (1)$$

where ΔS is the measured bending, L is the distance between laser beam points, t is the thickness, E is the Young's modulus, υ is the Poisson's ratio, and the subscripts of f and s respectively refer to film and substrate.

When the magnetostriction of fcc(001) single-crystal film is measured under a rotating magnetic field, a relationship among λ, λ_{100}, and λ_{111} is given[7] as the following formula,

$$\lambda = (3/2)\,\lambda_{100}\,[\alpha_1^2\,\beta_1^2 + \alpha_2^2\,\beta_2^2 + \alpha_3^2\,\beta_3^2 - (1/3)] + 3\,\lambda_{111}\,(\alpha_1\,\alpha_2\,\beta_1\,\beta_2 + \alpha_2\,\alpha_3\,\beta_2\,\beta_3 + \alpha_3\,\alpha_1\,\beta_3\,\beta_1)\,, \quad (3)$$

where α is the cosine of angle between the magnetization and the three crystallographic axes (a, b, c) and β is the cosine of angle between the direction of relative change in length and the axes. When the observation directions are fcc[100] and fcc[110], (β_1, β_2, β_3) values are respectively (1, 0, 0) and ($1/\sqrt{2}$, $1/\sqrt{2}$, 0), whereas (α_1, α_2, α_3) values are ($\cos\psi$, $\sin\psi$, 0) for both cases. Here, ψ is the angle of magnetization direction with respective to fcc[100]. By substituting α and β values to Eq. 2, the following relations are given,

$$\lambda = (1/4)\,\lambda_{100}\,(1 + 3\cos 2\psi)\,, \quad (3)$$

$$\lambda = (1/4)\,\lambda_{100} + (3/4)\,\lambda_{111}\sin 2\psi\,. \quad (4)$$

3. Results and Discussion

Figures 1(a)–(e) show the RHEED patterns observed for Ni(t_{Ni} nm)/$Ni_{50}Co_{50}$(100–t_{Ni} nm) films with different t_{Ni} values formed on Cu/Pd/MgO(001) substrates. Here, the incident electron beam is parallel to Cu[100] (‖ MgO[100]). Figure 1(f) shows the schematic diagram of diffraction pattern calculated for fcc(001) single-crystal surface with reconstructed structure of $c(2\times2)$. The observed diffraction patterns are in agreement with the simulated pattern. Therefore, Ni(t_{Ni} nm)/$Ni_{50}Co_{50}$(100–t_{Ni} nm) single-crystal films grow epitaxially on the underlayers. The crystallographic orientation relationship is determined as Ni(001)[100]$_{fcc}$ ‖ $Ni_{50}Co_{50}$(001)[100]$_{fcc}$ ‖ Cu(001)[100]$_{fcc}$. Figure 2 shows the $2\theta/\omega$-scan out-of-plane XRD patterns. fcc(002) and fcc(004) reflections from the Ni(t_{Ni} nm)/$Ni_{50}Co_{50}$(100–t_{Ni} nm) films are recognized around the diffraction angles, 2θ, of 51° and 122°, respectively. It is noted that fcc(004) reflections from the Ni and the $Ni_{50}Co_{50}$ layers are separately observed for the bi-layer films [Figs. 2(b)–(d)]. The result indicates that atomic mixing at the Ni/$Ni_{50}Co_{50}$ interface is not so high. The lattice constants of Ni layers in films with t_{Ni} = 25, 50, 75, and 100 nm are estimated to be 0.3514, 0.3516, 0.3518, and 0.3519 nm, whereas those of $Ni_{50}Co_{50}$ layers in films with t_{Ni} = 0, 25, 50, and 75 nm are calculated to be 0.3528, 0.3529, 0.3529, and 0.3528 nm, respectively.

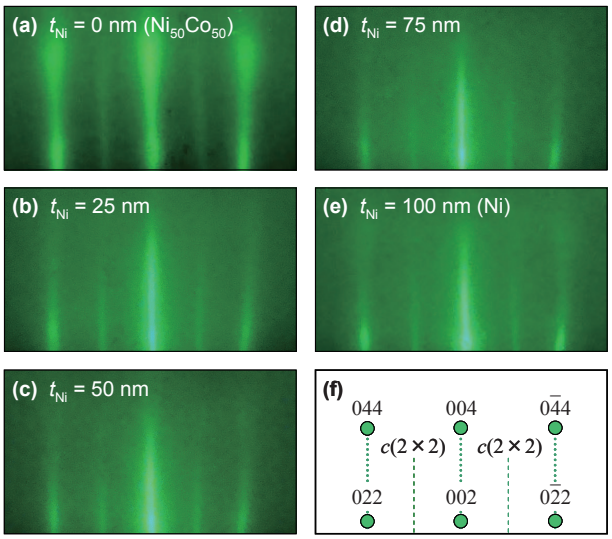

Fig. 1 (a)–(e) RHEED patterns observed for Ni(t_{Ni} nm)/$Ni_{50}Co_{50}$(100–t_{Ni} nm) films with t_{Ni} = (a) 0, (b) 25, (c) 50, (d) 75, and (e) 100 nm formed on Cu/Pd/MgO(001) substrates. (g) Schematic diagram of RHEED pattern simulated for fcc(001) single-crystal surface with reconstructed structure of $c(2\times2)$. The incident electron beam is parallel to (a)–(e) Cu[100] (‖ MgO[100]) or (f) fcc[100].

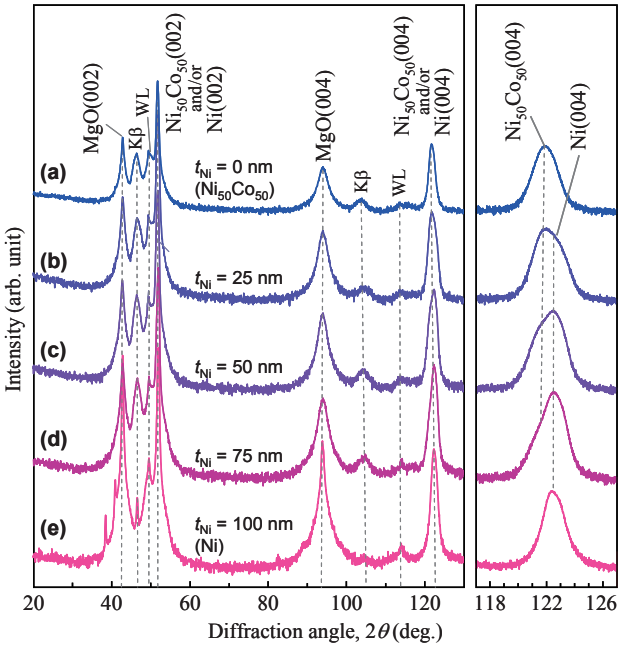

Fig. 2 Out-of-plane XRD patterns of Ni(t_{Ni} nm)/$Ni_{50}Co_{50}$(100–t_{Ni} nm) films with t_{Ni} = (a) 0, (b) 25, (c) 50, (d) 75, and (e) 100 nm formed on Cu/Pd/MgO(001) substrates. The intensity is shown in logarithmic scale. The small reflections noted as Kβ and WL are due to Cu-Kβ and W-Lα radiations included in the X-ray source, respectively.

These values are similar to the bulk values (a_{Ni} = 0.3524 nm[8], $a_{Ni_{50}Co_{50}}$ = (a_{Ni}[8] + $a_{fcc\text{-}Co}$[9])/2 = 0.3534 nm), suggesting that the strains in Ni and $Ni_{50}Co_{50}$ layers are small.

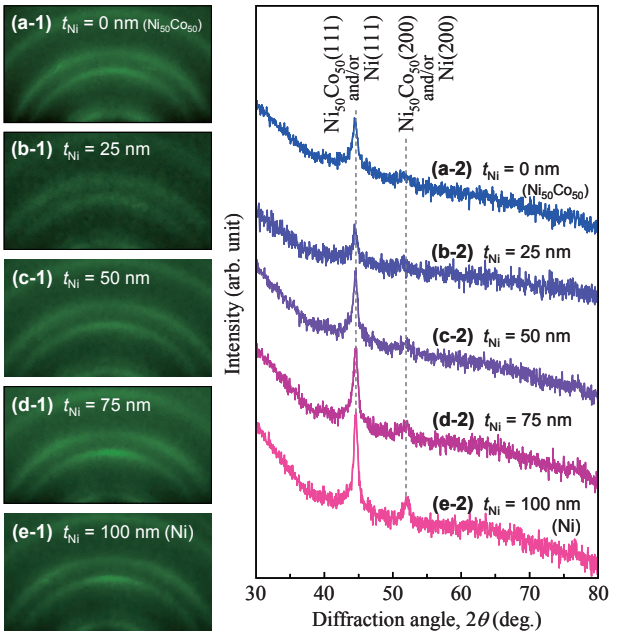

Fig. 3 (a-1)–(e-1) RHEED and (a-2)–(e-2) XRD patterns of Ni(t_{Ni} nm)/$Ni_{50}Co_{50}$(100–t_{Ni} nm) films with t_{Ni} = (a) 0, (b) 25, (c) 50, (d) 75, and (e) 100 nm formed on Cu/Pd/glass substrates. The XRD intensity is shown in logarithmic scale.

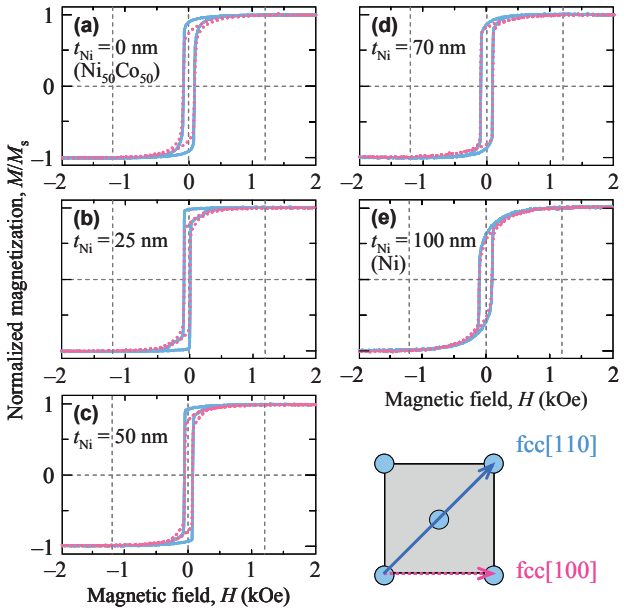

Fig. 4 Magnetization curves measured for Ni(t_{Ni} nm)/$Ni_{50}Co_{50}$(100–t_{Ni} nm) films with t_{Ni} = (a) 0, (b) 25, (c) 50, (d) 75, and (e) 100 nm formed on Cu/Pd/MgO(001) substrates. The vertical dotted lines show the strength of magnetic field (±1.2 kOe) used for magnetostriction measurements.

Figures 3(a-1)–(e-1) and (a-2)–(e-2), respectively, show the RHEED and the XRD patterns of Ni(t_{Ni} nm)/$Ni_{50}Co_{50}$(100–t_{Ni} nm) films formed on Cu/Pd/glass substrates. Ring-like RHEED patterns and XRD patterns showing fcc(111) and fcc(200) reflections are observed. The results show that poly-crystalline films with fcc structure are formed on glass substrates.

Figure 4 shows the in-plane magnetization curves of single-crystal films. The films are easily magnetized when the magnetic field is applied along fcc[110], whereas the magnetization curves measured along fcc[100] saturate at higher magnetic fields. There were no clear differences in the magnetization curves measured along fcc[100] and fcc[010] and measured along fcc[110] and fcc[$1\bar{1}0$] (not shown here). Therefore, the single-crystal films show four-fold symmetries in in-plane magnetic anisotropy, which is reflecting the magnetocrystalline anisotropy of fcc crystal with the easy magnetization axes parallel to fcc<111>. Figure 5 shows the magnetization curves of polycrystalline films. There were no differences in the curves measured along in-plane directions (not shown here). The poly-crystalline films show isotropic in-plane magnetic properties. The single- and poly-crystalline films are nearly saturated at a magnetic field of 1.2 kOe, which is used for magnetostriction measurements.

Figures 6(a) and (h) show the output waveforms of magnetostriction of $Ni_{50}Co_{50}$ (t_{Ni} = 0 nm) and Ni (t_{Ni} = 100 nm) single-crystal films measured along fcc[100]

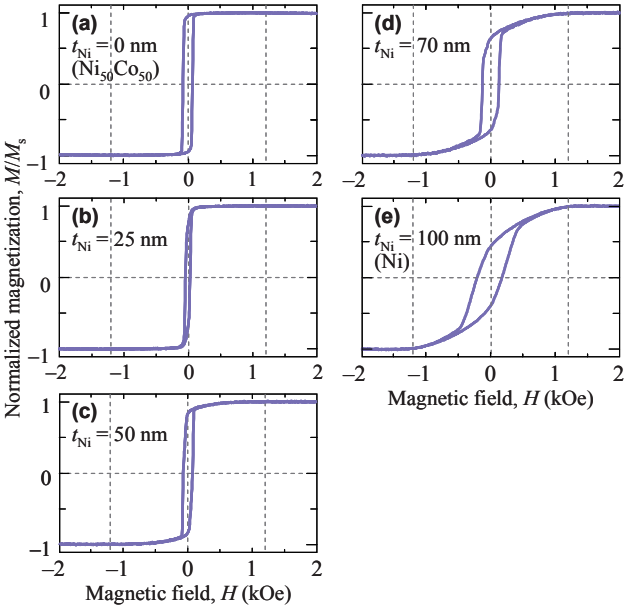

Fig. 5 Magnetization curves measured for Ni(t_{Ni} nm)/$Ni_{50}Co_{50}$(100–t_{Ni} nm) films with t_{Ni} = (a) 0, (b) 25, (c) 50, (d) 75, and (e) 100 nm formed on Cu/Pd/glass substrates. The vertical dotted lines show the strength of magnetic field (±1.2 kOe) used for magnetostriction measurements.

under the in-plane rotating magnetic field of 1.2 kOe, respectively. Phase of waveform is different between the two cases, suggesting that the $Ni_{50}Co_{50}$ and the Ni films have positive and negative λ_{100} values, respectively. Figures 6(a)–(d) show the output waveforms of

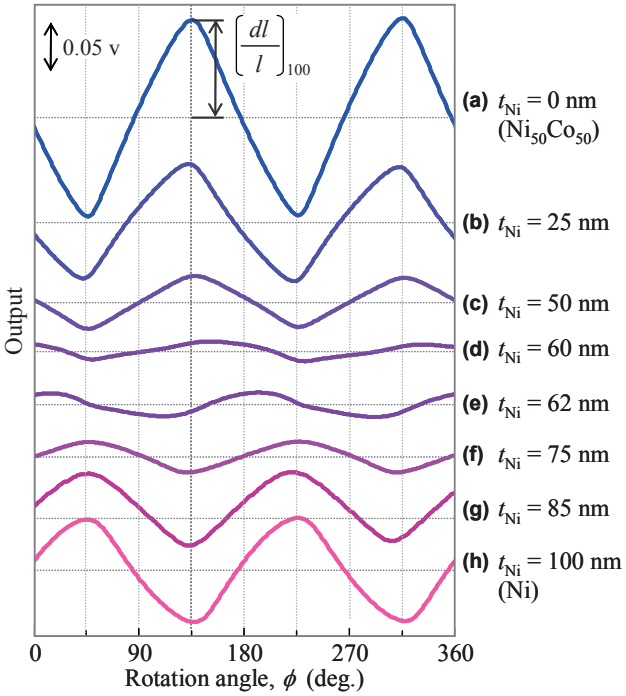

Fig. 6 Output waveforms of magnetostriction measured for Ni(t_{Ni} nm)/$Ni_{50}Co_{50}$(100–t_{Ni} nm) films with t_{Ni} = (a) 0, (b) 25, (c) 50, (d) 60, (e) 62, (f) 75, (g) 85, and (h) 100 nm formed on Cu/Pd/MgO(001) substrates. The observation direction is along fcc[100].

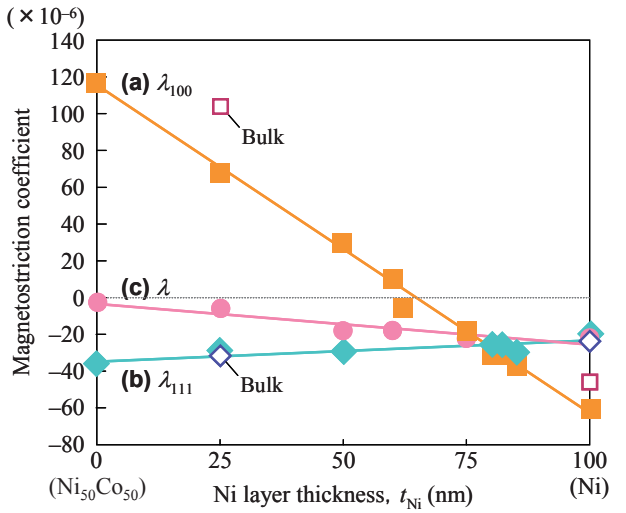

Fig. 7 Ni layer thickness dependences of (a) λ_{100}, (b) λ_{111}, and (c) λ values of Ni(t_{Ni} nm)/$Ni_{50}Co_{50}$(100–t_{Ni} nm) [(a), (b)] single- and (c) poly-crystalline films. The bulk values of λ_{100}, λ_{111}, and λ_s cited from Ref. 4.

single-crystal films with t_{Ni} = 0, 25, 50, and 60 nm. As t_{Ni} value increases from 0 to 60 nm, the amplitude of output gradually decreases, which indicates that the λ_{100} value decreases. The magnetostriction is apparently reduced by combing the $Ni_{50}Co_{50}$ crystal with positive λ_{100} value and the Ni crystal with negative λ_{100} value. Figures 6(d)–(f) show the waveforms of single-crystal films with t_{Ni} = 60, 62, and 75 nm. These films show

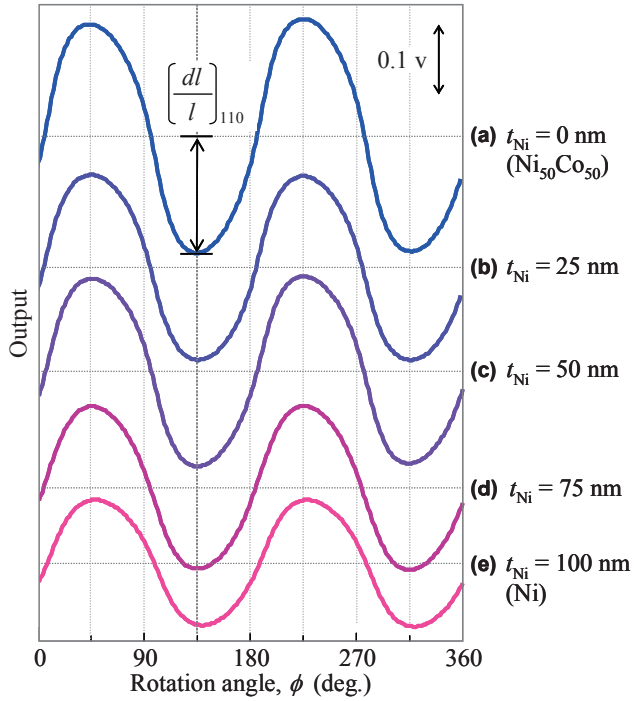

Fig. 8 Output waveforms of magnetostriction measured for Ni(t_{Ni} nm)/$Ni_{50}Co_{50}$(100–t_{Ni} nm) films with t_{Ni} = (a) 0, (b) 25, (c) 50, (d) 75, and (e) 100 nm formed on Cu/Pd/MgO(001) substrates. The observation direction is along fcc[110].

small amplitudes. The phase of waveform reverses with increasing t_{Ni} value from 60 to 75 nm. The sign of magnetostriction changes from positive to negative around t_{Ni} = 62 nm. Figures 6(f)–(h) show the waveforms of single-crystal films with t_{Ni} = 75, 85, and 100 nm. The amplitude increases with increasing t_{Ni} value. Figure 7(a) summaries the λ_{100} values of single-crystal films as a function of t_{Ni}. Here, the λ_{100} values are calculated by using Eq. 3. The λ_{100} value monotonically decreases from a positive value of $+1 \times 10^{-4}$ (t_{Ni} = 0 nm) to a negative value of -6×10^{-5} (t_{Ni} = 100 nm) with increasing t_{Ni} value. Figure 8 shows the waveforms of single-crystal films with different t_{Ni} values measured along [110]. The amplitude and the phase of waveform do not vary depending on t_{Ni} value. Figure 7(b) shows the variation of λ_{111} value as a function of t_{Ni}, where the λ_{111} values are calculated by using Eq. 4. The λ_{111} value slightly increases from -4×10^{-5} to -2×10^{-5}, as t_{Ni} value increases from 0 to 100 nm.

Figure 9 shows the waveforms of poly-crystalline films. As t_{Ni} value increases, the amplitude increases, though the phase dose not change. Figure 7(c) shows the λ values, which are estimated by using Eq. 1. The λ value decreases from -3×10^{-6} to -2×10^{-5} with increasing t_{Ni} value from 0 to 100 nm.

The present study demonstrates that reduction of

magnetostriction is possible by combining materials with negative and positive magnetostriction coefficients.

4. Conclusion

Single- and poly-crystalline Ni/$Ni_{50}Co_{50}$ bi-layer films are prepared by varying the layer thicknesses while keeping the total thickness at 100 nm. The effect of layer thickness ratio on the magnetostriction is investigated. The λ_{100} values of $Ni_{50}Co_{50}$ (t_{Ni} = 0 nm) and Ni (t_{Ni} = 100 nm) single-crystal films are positive (+1 $\times 10^{-4}$) and negative (-6×10^{-5}), respectively. As t_{Ni} value increases from 0 to 62 nm, the λ_{100} value decreases from positive to nearly 0. With further increasing t_{Ni} value, the λ_{100} value decreases to negative. On the other hand, the λ_{111} value remains almost similar (-4×10^{-5} to -2×10^{-5}). The λ value of poly-crystalline film decreases from -3×10^{-6} to -2×10^{-5} with increasing t_{Ni} value from 0 to 100 nm. The present study demonstrates that reduction of magnetostriction is possible by combining materials with negative and positive magnetostriction coefficients.

Acknowledgment A part of this work was supported by Chuo University Grant for Special Research.

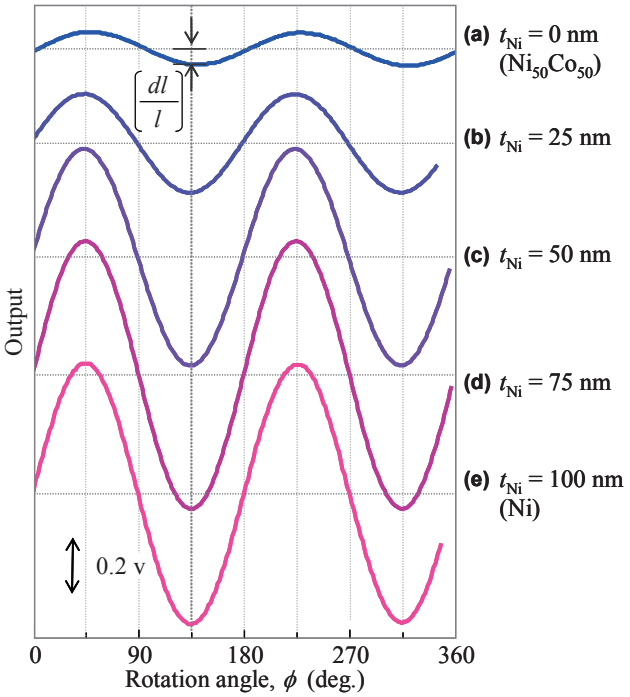

Fig. 9 Output waveforms of magnetostriction measured for Ni(t_{Ni} nm)/$Ni_{50}Co_{50}$(100–t_{Ni} nm) films with t_{Ni} = (a) 0, (b) 25, (c) 50, (d) 75, and (e) 100 nm formed on Cu/Pd/glass substrates.

References

1) H. A. M. de Gronckel, K. Kopinga, W. J. M. de Jonge, P. Panissod, J. P. Schillé, and F. J. A. den Broeder: *Phys. Rev. B*, **44**, 9100 (1991).
2) M. Ohtake, O. Yabuhara, J. Higuchi, and M. Futamoto: *J. Appl. Phys.*, **109**, 07C105 (2011).
3) K. Serizawa, T. Kawai, M. Ohtake, M. Futamoto, F. Kirino, and N. Inaba.: *IEEE Trans. Magn.*, **53**, 2004204 (2017).
4) S. Ishio, T. Kobayashi, H. Saito, S. Sugawara, and S. Kadowaki: *J. Magn. Magn. Mater.*, **164**, 208 (1996).
5) E. Klokholm: *IEEE Trans. Magn.*, **12**, 819 (1976).
6) T. Kawai, M. Ohtake, M. Futamoto: *Thin Solid Films*, **519**, 8429 (2011).
7) B. D. Cullity and C. D. Graham: *Introduction to Magnetic Materials* (Addision Wesley, Reading, MA, 1992).
8) M. Matsui and K. Adachi: *J. Magn. Magn. Mater.*, **10**, 152 (1979).
9) W. F. Schlosser: *Phys. Status Solidi A*, **17**,199 (1973).

Received Oct. 16, 2017; Accepted Mar. 21, 2018

J. Magn. Soc. Jpn., **42**, 83-89 (2018)

<Paper>

Effects of magnetic field applied during heat treatment on magnetic properties of non-oriented electrical steel sheets

T. Kinoshita, K. Kohara *, H. Shimoji **, T. Sato *, and T. Todaka *

Sumitomo Heavy Industries, Ltd., *19, Natsushima-cho, Yokosuka-shi, Kanagawa, 237-8555, Japan*

* Faculty of Science and Technology, Oita Univ., *700 Dannoharu, Oita, 870-1192, Japan*

** Dept. of Oita Industrial Research Institute., *4361-10, 1-chome, Takaenishi, Oita, 870-1117, Japan*

To improve the magnetic properties of non-oriented electrical steel sheets, the effects of applying heat treatment in a magnetic field on controlling the crystallographic orientation were studied. The heat treatment temperature was controlled to be 1023, 1123, and 1273 K. The magnetic field applied during the treatment was parallel to the rolling direction of sheet samples, and the magnetic field strength was 10 T at maximum. The samples heat treated in a magnetic field under the temperature condition of 1123 K or higher showed a remarkable change in magnetic properties as the textures changed. Even when a magnetic field was not applied, the grain growth was accelerated by heat treatment, iron loss was reduced, and permeability under low excitation conditions was improved. However, the permeability at 1.6 T or higher decreased. In this paper, it is shown that iron loss could be further reduced by applying a strong magnetic field during the cooling step of the heat treatment. It is also found that applying a strong magnetic field throughout the heat treatment, i.e. heating and cooling, inhibited grain growth, increased iron loss, and decreased magnetic permeability.

Key words: magnetic heat treatment, crystallographic orientation, iron loss

1. Introduction

There is an international demand for effective utilization of energy, especially for downsizing and improving efficiency of rotating electric motors (hereinafter referred to as electric motors), which account for a large proportion of total electric power consumption. The efficiency of electric motors is specified by the IEC standards, and the efficiency class is defined from the IE1 (standard efficiency) to the IE3 (premium efficiency). It is expected that demand for higher efficiency of electric motors will further increase in future.

Responding to the needs, effort to improve efficiency of electric motors and decrease energy losses, e.g. core losses, should be considered. Iron loss is known to increase due to the influence of residual stress during iron core processing, thereby deteriorating the magnetic properties. In order to reduce iron loss without changing the iron core material, it is expected that reduction or utilization of residual stress is necessary.

Strain relief annealing is an effective method to reduce residual stresses. In non-oriented electrical steel sheets, deterioration of magnetic properties due to processing strain is known to be improved by heat treating at about 1020 K[1]. However, strain relief annealing leads to texture changes within the material. A structure including hard axis of magnetization based on magneto-crystalline anisotropy appears in the plane of the electrical steel sheet, resulting in the deterioration of magnetic properties at 1.5 T or higher. Thus, it may not be possible to take full advantage of material properties with simple heat treatment[2,3]. Therefore, the authors' group has studied heat treatment in a magnetic field which offers the possibility of controlling the texture of the magnetic material during heat treatment.

It is well known that magnetic properties of magnetic materials are improved by heat treatment in a magnetic field[4], In addition, some literatures reported that the material's texture could be controlled with such heat treatment processes [5,6]. However, there are few detailed reports on the magnetic properties under alternating excitation of non-oriented electrical steel sheets heat-treated in a magnetic field. Moreover, detailed mechanism of the phenomenon is not well understood and there are only a few reports on their industrial application. The authors in present study investigated the effects on the magnetic properties under alternating excitation of samples heat-treated in a magnetic field by using commercially available electromagnetic steel plates. In our previous reports, samples of sufficient size could not be produced due to the structural

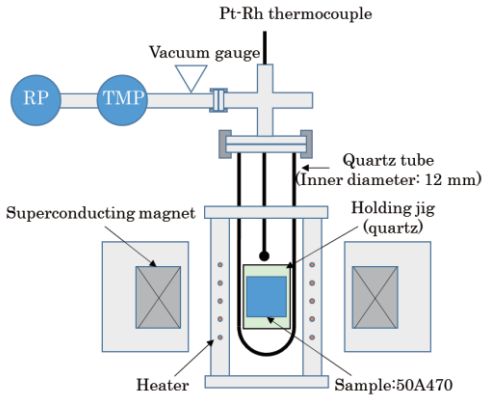

Fig. 1 Schematic diagram of magnetic heat treatment apparatus.

constraints of heat treatment equipment, and there was only qualitative discussion[7]. Subsequently, quantitative evaluation methods of samples with shape constraints were studied, and the magnetic properties in the direction of the magnetic field applied during heat treatment were measured with a small-sized single sheet tester (SST) [8]. In this paper, by comparing magnetic properties with and without a magnetic field during heat treatment, we make clear quantitatively magnetic properties depending on heat treatment conditions, i.e. temperature and magnetic field.

2. Experimental method and apparatus

2.1 Heat treatment apparatus in a magnetic field

Fig. 1 shows a schematic view of the heat treatment apparatus. The heat treatment apparatus in a magnetic field consisted of a superconducting magnet (10 T-CSM) with an inner diameter of 100 mm, and a quartz glass tube with outer diameter of 14 mm and inner diameter of 12 mm of which one end was closed. The quartz glass tube was inserted into an electric furnace with an outer diameter of 50 mm and an inner diameter of 22 mm. The structure could be depressurized to less than 10^{-3} Pa with a turbo molecular pump. Samples were prepared by cutting a non-oriented electrical steel sheet 50A470 (JIS C 2552) to 10 mm × 50 mm by electrical discharge machining, and set at the center of the magnetic field in the quartz tube using a holding jig made of quartz so that the field direction of the magnetic field was parallel to the longitudinal direction of the sample. Thus, the uniformity of the magnetic field during the heat treatment at the sample position was sufficiently maintained. The temperature around the sample was measured using a Pt-Rh thermocouple.

Fig. 2 shows the temperature profile and applied magnetic field pattern. In this test, the temperature was raised to the set temperature at a rate of T/t_1 = 500 K/hr, and after reaching the set temperature, the sample was held for $(t_2 - t_1)$ = 1 hr, and then cooled to room temperature at a rate of $T / (t_3 - t_2)$ = 100 K/hr. A constant magnitude of magnetic field was kept throughout the heating and cooling cycle until the sample was cooled to room temperature.

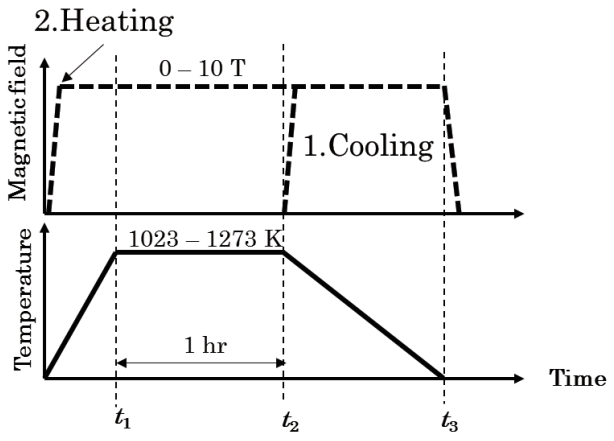

Fig. 2 Schematic diagram of magnetic field during heat treatment.

2.2 Small-sized Single Sheet Tester (SST) [8]

Fig. 3 shows the measurement system of SST, and Fig. 4 shows the schematic diagram of the apparatus configuration. As an excitation coil, polyester copper wire (PEW), ϕ1.0 mm, was wound for 380 turns on the epoxy resin frame. As a yoke, 20 electrical steel sheets (50A470) cut out by electrical discharge machining were used, and laminated and adhered in the direction of the paper surface of Fig. 3 to a thickness of 10 mm or more. By using the stacked yokes, leakage of magnetic flux is prevented and generation of eddy currents is reduced. Samples were formed by electrical discharge machining of electrical steel sheets (50A470) to be 10 mm × 50 mm, with the rolling direction being the longitudinal direction of the sample. A measurement sample placed in the central part of the excitation coil is excited by alternating magnetic flux in the longitudinal direction to measure the alternating magnetic properties of 50Hz. As shown in Fig. 3, feedback control can be performed in this system, and a sinusoidal magnetic flux density waveform in the sample is maintained. The magnetic flux search coil (B-coil), of 3 turns is wound at the central portion of the sample, and the magnetic flux

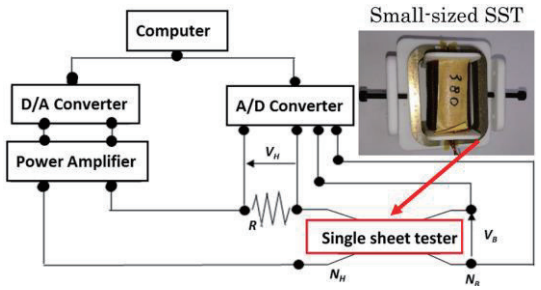

Fig. 3 System for measuring magnetic properties of SST.

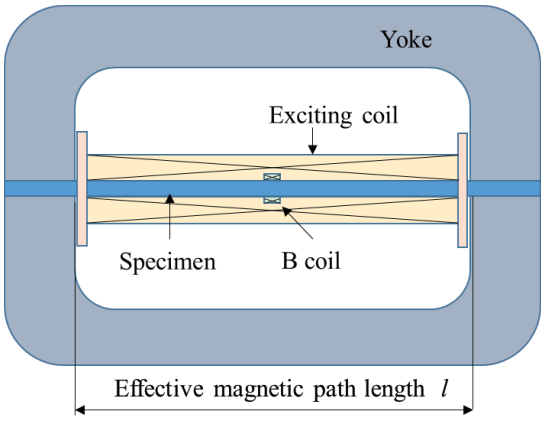

Fig. 4 Schematic diagram of SST configuration.

density B is thereby detected. The magnetic field strength H is calculated from the excitation current detected by the shunt resistance. The effective magnetic path length l is determined as the yoke inner dimension (40 mm). Based on the above conditions, multiple samples were measured a number of times, and the average value was taken as the measurement result.

3. Experimental results and discussion

3.1 Effect of heat treatment temperature

To understand the effects of heat treatment in a magnetic field on the magnetic properties of the electrical steel sheets, heat treatment in the absence of a magnetic field was firstly carried out. The heat treatment temperatures for comparison were 1023, 1123, and 1273 K. Samples were heated at 330 K/hr, held for 1 hr, and then cooled to room temperature at 100 K/hr. Same cooling and heating rate was used regardless of the heat treatment temperature. Fig. 5 shows the iron loss measurement results of the samples fabricated at each heat treatment temperature. It was found that the iron loss decreased under all conditions as compared with ones before heat treatment. In addition, the iron loss also decreased as the heat treatment temperature increased. Next, magnetic permeability characteristics depending on the heat treatment temperature were investigated. Fig. 6 shows the measurement results of the magnetic permeability. Compared with the relative permeability of the electrical steel sheets before heat treatment, the relative permeability increased with the excitation magnetic flux density of 1.5 T or less under all the temperature conditions. In addition, the magnetic permeability increased as the heat treatment temperature increased. Reduction of the iron loss and increase of the relative permeability may be attributed to grain growth[9].

Fig. 7 shows an image of crystal grains observed with an optical microscope. As expected, the crystal grains became coarser compared with those before heat treatment. The grain size of the sample heat-treated at 1273 K increased to nearly 1 mm. Thus, the increase of the magnetic permeability can be explained by the relative reduction of crystal grain boundary areas, which constitute an energy barrier, resulting in the reduction of iron loss due to facilitated magnetic domain wall movement. As for the excitation magnetic flux density of 1.6 T or higher, the iron loss was reduced, but the magnetic permeability decreased as compared with that before heat treatment. The reason that the permeability decreases in the high magnetic field of ≥1.6 T is due to the fact that the 90° magnetic domains with respect to the excitation direction are increased by the heat treatment. Normally the <100> direction, i.e. the easy direction of crystal magnetization, is largely distributed within the plane in order to reduce spontaneous magnetization in thickness direction. However the heat treatment promoted isotropic grain growth resulting in increased <100> crystals in the

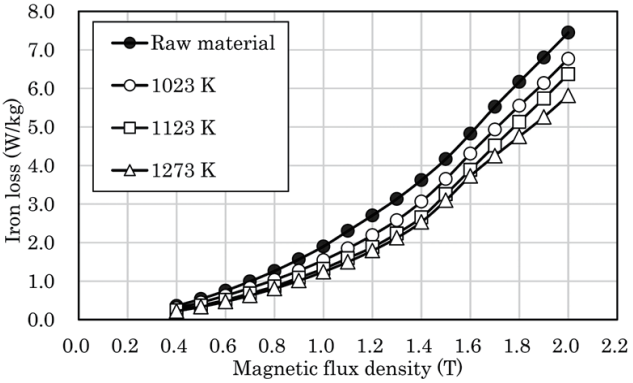

Fig. 5 Iron loss properties of heat treated samples.

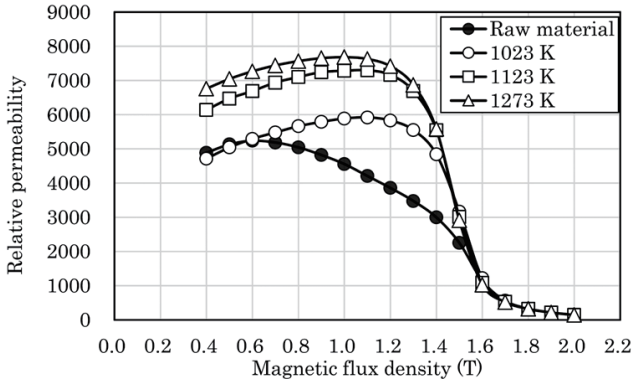

(a) Results of measuring relative permeability.

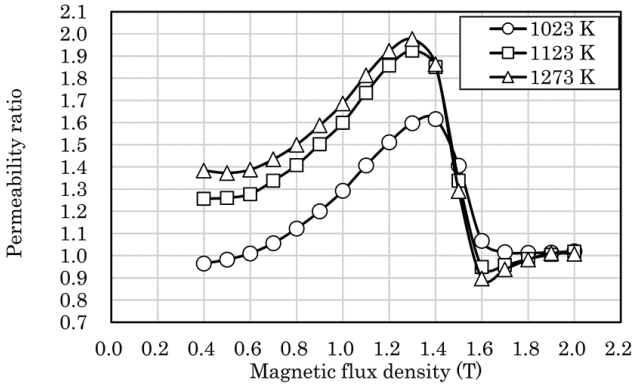

(b) Magnetic permeability change in heat treated samples with respect to magnetic permeability before heat treatment.

Fig. 6 Magnetic permeability properties of heat treated samples.

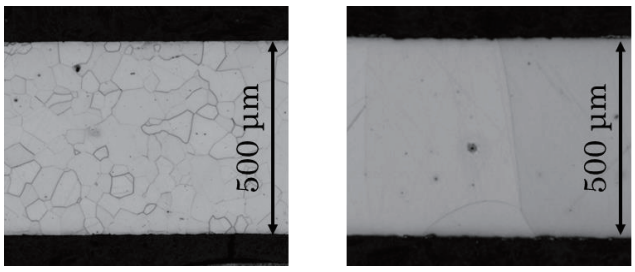

(a) 1023 K (b) 1273 K

Fig. 7 Crystal grain of specimen section observed by using optical microscope.

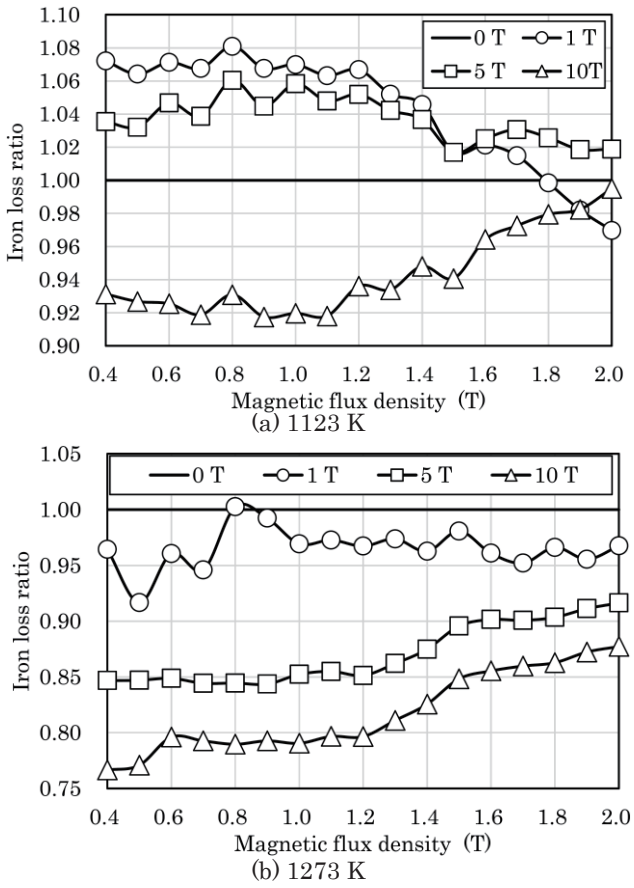

Fig. 8 Change rate of iron loss characteristics of samples heat treated in magnetic field.

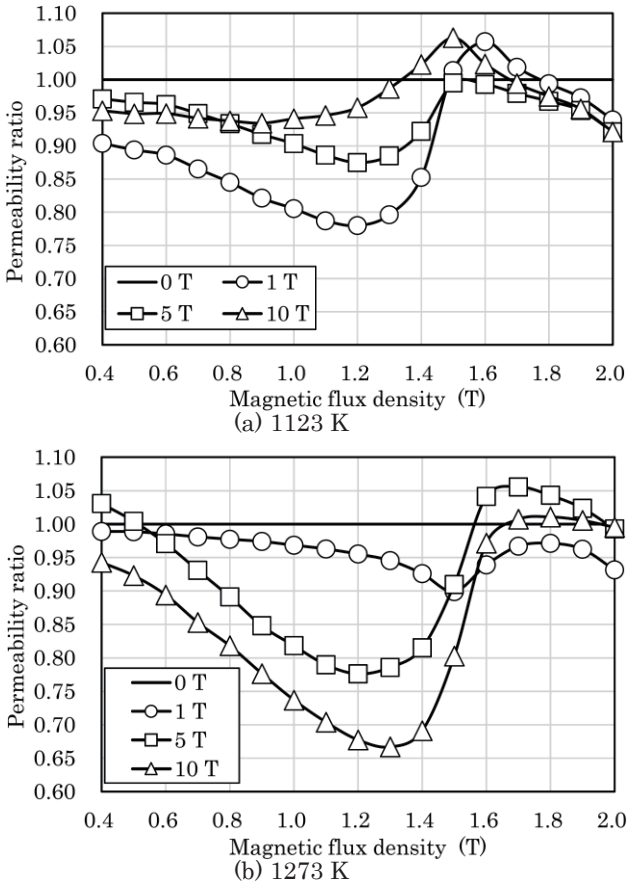

Fig. 9 Change rate of magnetic permeability characteristics of samples heat treated in magnetic field.

thickness direction.

3.2 Effect of magnetic field during cooling process

It was found that the magnetic properties of electrical steel sheets subjected to simple heat treatment deteriorated at the exciting magnetic flux density of ≥1.6 T. The reason for poor properties is the spontaneous magnetization in the thickness direction of the steel sheet due to isotropic grain growth. Therefore, by applying a magnetic field during heat treatment, spontaneous magnetization in the thickness direction of the steel sheet is expected to be suppressed, resulting in good magnetic properties even in a high excitation field.

The anisotropy induced by heat treatment of soft magnetic materials in a magnetic field is often explained in terms of magnetic atom pair ordering mechanism. According to the model for binary alloys proposed independently by Néel[10] and Taniguchi[11], the directional diffusion takes place with a preferred direction of magnetic atom pairs imposed by the direction of magnetization during the heat treatment and/or subsequent cooling. This explanation should be applied to materials with directional-ordered crystallographic microstructure. Since, the material used in this study has a few percent of silicon and it is seldom the ordered lattice structure, the above model is not considered to be dominant. A previous study reported that texture could be controlled by applying a magnetic field to electrical steel sheets during the cooling step of the heat treatment[12]. Hence, the application of magnetic field during cooling step improves the magnetic properties of electrical steel sheets. In the present study, the heat treatment temperature of the sample was set to 1123 K and 1273 K at which the iron loss reduction effect was particularly marked, and a magnetic field was applied during cooling. The applied magnetic field strength was set to 1 T, 5 T, 10 T, and the effects of the heat treatment temperature and the magnetic field strength applied during cooling on magnetic properties were investigated. Fig. 8(a) shows the changing rate of iron loss characteristics of the samples heat-treated at 1123 K in a magnetic field relative to one of the sample heat-treated in the absence of a magnetic field. At 1 T and 5 T, the iron loss increased with its ratio greater than 1, but at 10 T, the iron loss was reduced in all regions. Although the detailed mechanism is not completely understood, the application of a magnetic field during cooling clearly affected the magnetic properties. In the sample subjected to heat treatment in a magnetic field at 1273 K, as shown in Fig. 8(b), the iron loss is reduced in almost all regions by applying the magnetic field. Although at 1123 K, a correlation with the magnetic field strength was not confirmed, at 1273 K it was found that iron loss could be further reduced by increasing the magnetic field strength. This experimental result suggests that raising the heat treatment temperature increases the sensitivity of the sample to the magnetic field.

Next, the change in the relative permeability due to heat treatment in the magnetic field was examined. Fig. 9(a) shows the measurement result of the changing rate of the relative magnetic permeability of the sample heat-treated in the magnetic field at 1123 K, and Fig. 9(b) shows the result at 1273 K. As seen from Fig. 9(a), at ≤1.3T, the relative magnetic permeability of the samples heat-treated in the magnetic field decreased, and the decrease rate of the sample heat-treated at 1 T is the largest. Although a slight increase in magnetic permeability was observed between 1.4 T and 1.6 T, the relative permeability ratio at ≥1.8 T decreased to less than 1. In Fig. 9(b), by applying a magnetic field (neglecting 1 T), the magnetic permeability decreased in the sample heat-treated at 1273 K under relatively low excitation conditions and increased under high excitation conditions. The behavior of this relative permeability was observed independently at different temperature in heat treatment. However, the changing rate of the relative permeability with respect to the magnetic field was larger at higher temperature i.e. 1273 K. Similar to iron loss, the sensitivity of magnetic properties to the magnetic field during heat treatment is higher for samples heat treated at high temperature.

The change in magnetic properties could be possible due to change in texture of the sample caused by application of the magnetic field during heat treatment. In order to evaluate the texture of a sample heat-treated in the magnetic field, X-ray pole figure measurement was performed. Fig. 10 shows the {110} X-ray pole figure measurement results for the samples (a) before heat treatment, and (b), (c), after heat-treated at 1123 K and 1273 K, respectively. In Fig. 10, the region enclosed by the red line is a strong intensity position, indicating the presence of a texture. At 1123 K, only minor changes were found compared with before heat treatment. At 1273 K, the texture was greatly changed and high intensity diffraction lines could be seen at the center of the {110} pole figure, indicating that {110} increased in the plane parallel to the surface of the steel sheet. Since

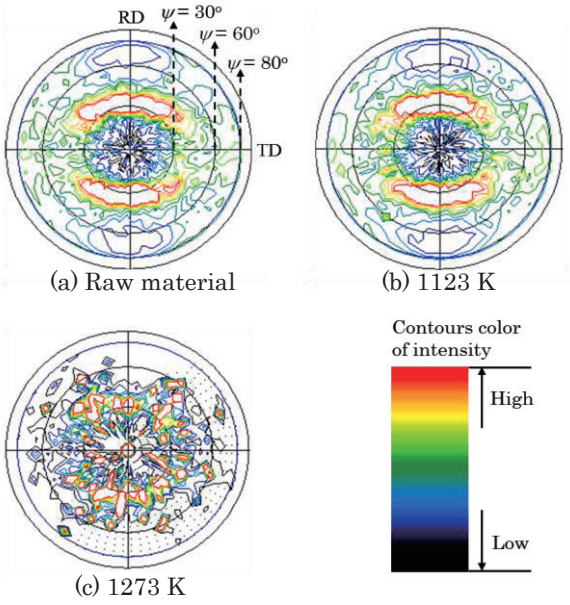

Fig. 10 {110} pole figure analysis of magnetic heat-treated non-oriented electrical steel sheet.

{110} is the plane orientation including both the <100> direction which is the easy magnetization direction and the <111> direction which is the hard magnetization direction, it is expected that magnetization properties improved in the <100> direction. However, in the longitudinal direction of the sample which is the measurement direction, i.e. in the direction of the magnetic field during heat treatment, improvement of magnetization properties could not be confirmed. The induced magnetic anisotropy in the non-oriented electrical steel sheets is considered to be a large influence of crystal orientation. The sample subjected to heat treatment in the magnetic field undergoes a recrystallization process accompanied with preferred orientation, whereby the crystal orientation distribution changes and anisotropy appears. As the conditions under which the anisotropy was induced, in the present experiments, both of a sufficient temperature condition for causing recrystallization and a strong magnetic field capable to give non-negligible influence on the scattering by the temperature are necessary. We believe, by clarifying the relationship between magnetic field applied during heat treatment and the resulting crystal orientations, crystal directions that improve magnetic properties of steels could be determined and preferentially textured within the material.

3.3 Effect of magnetic field applied during heating

An electrical steel sheet made of iron to which a few percent of silicon is added becomes a paramagnetic substance at and above the Curie temperature. The sheet does not exhibit spontaneous magnetization, suggesting that it is not likely to easily get affected by a magnetic field above the Curie temperature. However, Bacalchuk et al. reported that application of a magnetic field in the temperature range showing paramagnetism was effective to control texture[13]. In addition, by applying a magnetic field in the ferromagnetic state, individual crystal grains may generate magnetostriction and expand or contract according to the crystal orientation. An energy barrier is then formed at the crystal grain boundaries which interferes with grain growth[14,15], resulting in deterioration of magnetic properties. Hence, the effects of the magnetic field may not necessarily be obtained under ferromagnetic conditions in soft magnetic materials against that magnetic properties are expected to improve by heat treatment in a magnetic field. As described in the previous section, the effects of the magnetic field are more pronounced when applied during heat treatment at ≥1123 K, which is believed to exceed the Curie temperature. Therefore, by comparing the magnetic properties of a sample to which a magnetic field was applied only during the cooling to a sample produced by continuous application of a magnetic field throughout heating and cooling, we examined the heat treatment condition under which the magnetic field was more effective with respect to material's magnetic properties. The measurement condition are selected to be 1 T and 10 T at 1273 K of which the effects of the magnetic field

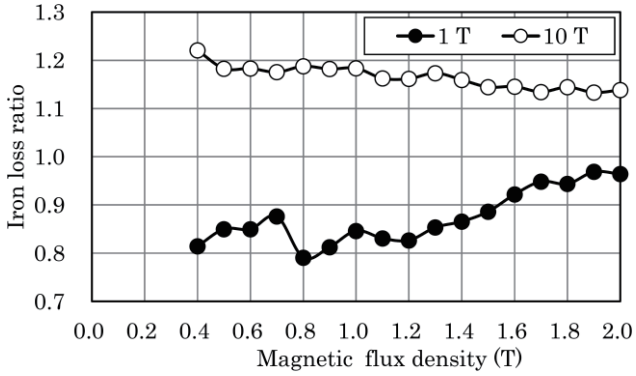

Fig. 11 Change rate in the iron loss of the sample applied throughout heating and cooling to one of the sample applied the same magnetic field strength during cooling at 1273 K.

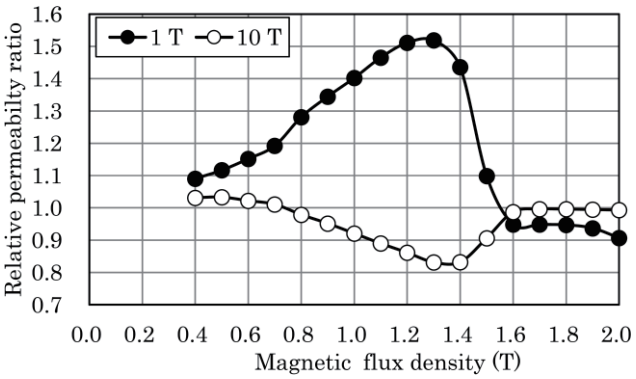

Fig. 12 Change rate in the magnetic permeability of the sample applied throughout heating and cooling to one of the sample applied the same magnetic field strength during cooling at 1273 K.

during cooling is particularly observed in the previous section.

Fig. 11 shows the iron loss characteristics of the sample in which the magnetic field was applied during heating. The magnetic field strength during the heat treatment was maintained at 1 T and 10 T. Reported iron loss values are relative to those of the samples in which the magnetic field was applied only during cooling. It is seen that with at the magnetic field of 1 T, the iron loss was reduced by applying the magnetic field throughout during heat treatment. Regarding magnetic permeability, as seen in Fig. 12, the permeability was improved by about 50 % under an excitation condition of ≤1.5 T. This is believed to be the result of crystal growth during heat treatment under the magnetic field. The reason why the magnetic permeability decreased at ≥1.6 T is because of the increase in the 90° magnetic domain as mentioned previously. On contrary, heat treatment with applied magnetic field of 10 T led to iron loss increase of 13 % in comparison with that when the magnetic field was applied during cooling only. However, with increasing magnetic flux density, magnetic permeability ratio decreased in the range of 0 to 1.5 T.

3.4 Consideration on effect of magnetic field annealing

The following two reasons can be considered as reasons why the magnetic properties were deteriorated in the sample when the magnetic field was applied throughout heat treatment, compared with that of the sample when the magnetic field was applied during cooling. Firstly, sufficient grain growth may not have been achieved under the influence of the magnetic field. This could be because the crystal grains in the electrical steel sheet expand or contract due to magnetostriction and form an energy barrier in the crystal grain boundary. The second reason may be an increase in the 90° magnetic domain. It is known that when a soft magnetic material is heat-treated in a magnetic field, its magnetic domain structure changes remarkably[16]. Since λ_{111} which is a typical magnetostriction constant of iron is a negative value[17], the sample may contract in the magnetic field direction if a strong magnetic field is applied at a temperature below the Curie temperature. By maintaining the contracted state while being exposed to a high temperature, crystal grains grow with a relatively large number of 90° magnetic domains, resulting in microstructural texturing. We believe that this phenomenon would be better understood and explained in future works by detailed observation of crystal grains and boundaries inside the sample and observing the changes in magnetic domains. Furthermore, in addition to the magnetic field application conditions verified in this paper, experiments will be carried out the application of a magnetic field only during heating up to certain temperature and only during keeping, we make clear a suitable heat treatment condition, which is most effective to material's magnetic properties.

4. Conclusion

In this paper, the effects of heat treatment in an applied magnetic field on the magnetic properties of the commercial electrical steel sheet (50A470) were reported. Upon heat treating in the absence of magnetic field, grain growth was promoted and iron loss was reduced with increasing heat treatment temperature. The relative permeability, however, decreased at the alternating excitation condition of ≥1.6 T. The magnitude of the influence of the magnetic field varied with heat treatment temperature, and greater effects were seen at higher temperature. These effects also varied depending on whether the magnetic field was applied throughout the heat-treatment or during cooling alone. Iron loss was seen to increase and magnetic permeability decrease with 10 T magnetic field applied throughout heating and cooling, as compared with 10 T applied during cooling only. The results demonstrate that the strength of magnetic field and whether the magnetic field is applied during cooling or throughout the heat treatment process are both important parameters.

Results confirmed the change in texture of non-oriented electrical steel sheet due to heat treatment in magnetic field, ultimately affecting the magnetic properties under alternating excitation. In future works, we will clarify the phenomenon whereby the magnetic properties change due to heat treatment in a magnetic field by analyzing detailed observation of crystal orientation distribution and crystal grain boundaries using EBSD or XRD, by observing the change of magnetic domain structures using Kerr effect, and by measuring the two-dimensional magnetic properties.

Acknowledgements The heat treatment samples in the magnetic field in this paper were the result of a joint use study (Issue No. 16H0066) of the High Field Laboratory for Superconducting Materials attached to Institute of Materials Research, Tohoku University. We would like to thank Kohki Takahashi, Associate Professor, for his collaboration with this research, from whom we received valuable advice on sample fabrication.

References

1) JFE Steel Corporation, ELECTRICAL STEEL SHEETS, p.21 (2010).
2) A. Kutsukake, Y. Kido, T. Ikeda, T. Kinoshita, T. Todaka., The Papers of Technical Meeting on Magnetics, IEE Japan, **MAG-16-086** (in Japanese), pp.23-28 (2016).
3) M. Wada: National Technical Report, **50**, pp.878-882 (1984).
4) S. Koshiba et al.: Hitach Review, **16**, pp.1-5 (1956).
5) N. Masahashi, M. Matsuo, K. Watanabe: *J. Mater. Res.*, **13**, pp.457-461 (1998).
6) H. O. Martikainen and V. K. Lindroos: *Scandinavian J. Metallurgy*, **10**, pp.3-8 (1981).
7) T. Kinoshita, T. Todaka, H. Shimoji, T. Sato: *J. Jpn. Soc. Applied Electromagnetics and Mechanics* (in Japanese), **25**, pp.162-167 (2017).
8) T. Kinoshita, K. Kouhara, H. Shimoji, T. Sato, T. Todaka, The Papers of Technical Meeting on Magnetics, IEE Japan, **MAG-17-083** (in Japanese), p.25 (2017).
9) H. Denma, Y. Ishihara, T. Todaka, M. Doi: *J. Magn. Magn. Mater.*, **215-216**, pp.106-109 (2000).
10) L. Néel: *J. Phys. Radium*, **15**, pp.225-239 (1954).
11) S. Taniguchi, M. Yamamoto: *Sci. Rept. Res. Inst. Tohoku Univ.*, **A6**, p.330 (1954).
12) H. Komei, *Trans. JIM.*, **9**, pp.88-92 (1968).
13) C.M.B. Bacaltchuk, G.A. Castello-Branco, M. Ebrahimi, H. Garmestani and A.D. Rollett: *Scripta Mater.*, **48**, pp.1343-1347 (2003).
14) T. Watanabe, T. Suzuki, S. Tanii, H. Oikawa: *Phil. Mag. Lett.*, **62**, pp.9-7 (1990)
15) Y. Xu, H. Ohtsuka, K. Ito, H. Wada, *J. Magn. Soc. Jpn.* (in Jananese), **24**, pp.651-654 (2000).
16) J. Marcin et al.: Acta Electorotechnica et Informatica, **13**, DOI: 10.2478/aeei-2013-0020 (2013).
17) S. Chikazumi: "Physics of Ferromagnetism", **2**, p.125 (Syokabo, Tokyo,1974).

Received Nov. 22, 2017; Revised Jan. 23, 2018; Accepted Feb. 14, 2018

J. Magn. Soc. Jpn., **42**, 90-95 (2018)

<Paper>

Optimization of Resonant Circuit and Evaluation of Magnetic Field Uniformity with 50 mm Gap Magnetic Field Generator

R. Hasegawa, T. Nakagawa, S. Seino and T. A. Yamamoto

Graduate School of Engineering, Osaka University, *2-1 Yamadaoka, Suita, Osaka 565-0871, Japan*

Heating mediators for magnetic hyperthermia treatment (MHT) are dependent on magnetic field strength. Therefore, a hyperthermia applicator that generates a homogeneous magnetic field is required. We fabricated a 50 mm gap magnetic field generator (hereinafter called the 50 mm prototype), and the guideline for optimizing combination of parameters of the resonant circuit was suggested to maximize the estimated heating index (product of frequency and magnetic field strength). We found that a 7×2-turn coil is optimal for the 50 mm prototype. We consider that this optimization method is applicable for designing a full-scale hyperthermia applicator. The uniformity of magnetic field strength distribution in the 50 mm prototype was measured by a pickup coil, and we show experimentally that magnetic circuit type magnetic field generator is appropriate for the MHT applicator. The feasibility of a full-scale MHT applicator was increased by the suggestion of guideline for high-estimated heating index operation and the demonstration of magnetic field homogeneity.

Key words: hyperthermia, magnetic field generator, magnetic circuit, resonant circuit, uniform magnetic field

1. Introduction

Hyperthermia therapy has gained attention in recent years as a new cancer treatment. In current clinical practice, it is performed with induction heating in the radio frequency range (8 MHz or 13.56 MHz) and dielectric heating in the microwave range (430 MHz or 2450 MHz) [1]. In this study, we focused on magnetic hyperthermia treatment (MHT), which can heat the cancer tissue locally using relatively low frequencies (100 kHz to 1 MHz). The treatment procedure is as follows. A heating mediator such as an electrical conductor [2], magnetic fluid [3], or bulk magnetic material [4] is inserted around the cancer tissue. An alternating magnetic field is applied to the heating mediator from outside the body and the mediator is heated by eddy-current loss, Neel and Brownian relaxations, or hysteresis loss. The target temperature of the heating mediator is between 42 and 45 °C [5) 6)].

The specific absorption rate (*SAR*) of heating mediators is proportional to the magnetic field strength to a power of between 1.5 and 2.3 [3) 6)-8)]. As magnetic field strength has a large influence on *SAR*, a homogeneous magnetic field is required and the heating mediator must be capable of being heated correctly anywhere in the body. Therefore, a hyperthermia applicator is required to generate a homogeneous (±5%) magnetic field over a large area (5–10 L [5)]). Additionally, for the widespread adoption of MHT, it is desirable that the hyperthermia applicator should be as simple as possible. However, a full-scale MHT applicator requires a large-capacity power supply. This is why that a MHT applicator that operates on condition of high-estimated heating index is required. Estimated heating index is product of frequency and magnetic field strength and in proportional to *SAR* of heating mediator.

The guideline for high-estimated heating index operation is required when designing a full-scale MHT applicator. There has been no study that focuses on estimated heating index and no suggestion about the guideline for optimizing resonant circuit of MHT applicator. We consider that optimizing resonant circuit improves estimated heating index of MHT applicator. We evaluated the resonant characteristics with the 50 mm prototype. Assuming that *SAR* is proportional to the product of frequency and magnetic field strength, the guideline for optimizing circuit parameters that maximize estimated heating index was suggested. Moreover, we applied this guideline to 50 mm prototype and confirmed that the optimal resonant circuit parameter was uniquely determined. This guideline is helpful for designing a full-scale MHT applicator.

In previous research, it has been shown that magnetic field uniformity in the magnetic circuit type magnetic field generator by the electromagnetic field analysis[9)]. In this paper, we experimentally demonstrated magnetic field uniformity in the 50 mm prototype to consolidate validity of the magnetic circuit type magnetic field generator. By the suggestion of the guideline for high-estimated heating index operation and the experimental demonstration of magnetic field uniformity, the feasibility of a full-scale MHT applicator was improved.

2. Experiment equipment

As a preliminary stage for fabrication of a full-scale MHT applicator, we fabricated a prototype that has 50 mm gap and magnetic poles with a cross-sectional area of 90×90 mm^2 (Fig. 1). The purpose of this prototype is the evaluation of the resonant circuit, the verification of the guideline for optimizing the resonant circuit and the demonstration of magnetic field uniformity. Too narrow gap makes it difficult to measure the magnetic field distribution. To evaluate the magnetic field

distribution by the multi-point with a pickup coil (spatial resolution: x-axis 1.3 mm, y-axis 10 mm, z-axis 10 mm), the gap width was 50 mm. The circuit was composed of a pair of E-type ferrite cores (TDK, PC40), and excitation coils were wound about the magnetic poles. The pair of excitation coils was connected in series. We refer to the number of turns of the coil as (number of turns on one side) × 2. The excitation coil was composed of copper pipe (inner diameter 2 mm and outer diameter 3 mm) to circulate cooling water.

Fig. 2 shows the simplified equivalent circuit of the resonant circuit. L_c, C_c are inductance (L_c =0.9 μH) and capacitance (C_c =360 pF) of the 50 Ω coaxial cable. AC resistance of excitation coil R_e was only considered as resistance component because it has the most significant influence on impedance characteristic. The combined impedance between terminals A and B is expressed by Eq. (1). The impedance between terminals A and B was measured using an LCR meter (HIOKI, 3532-50).

$$Z = \mathrm{Re}\{Z\} + j\mathrm{Im}\{Z\} = \frac{\alpha\gamma + \beta\delta}{\gamma^2 + \delta^2} + j\frac{\beta\gamma - \alpha\delta}{\gamma^2 + \delta^2}$$

$$\begin{cases} \alpha = -\omega^2 L_m R_e (C_c + C_m) \\ \beta = -\omega^3 L_m (L_e + L_c)(C_c + C_m) + \omega L_m \\ \gamma = \omega^4 L_m (L_e + L_c) C_m C_c \\ \qquad - \omega^2 \{L_m C_m + (L_e + L_c)(C_c + C_m)\} \\ \delta = -\omega^3 L_m C_m C_c R_e + \omega R_e (C_c + C_m) \end{cases} \quad (1)$$

The excitation current I_e is expressed Eq. (2).

$$|I_e| = \frac{VC_m}{\sqrt{\{R_e(C_c + C_m)\}^2 + \left\{\omega(L_e + L_c)(C_c + C_m) - \frac{1}{\omega}\right\}^2}} \quad (2)$$

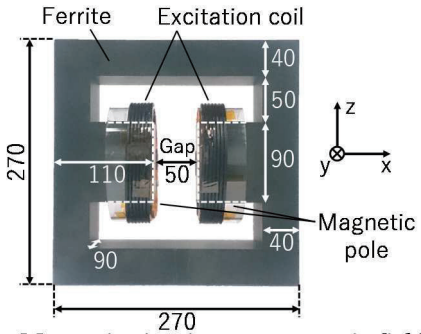

Fig. 1 Magnetic circuit type magnetic field generator.

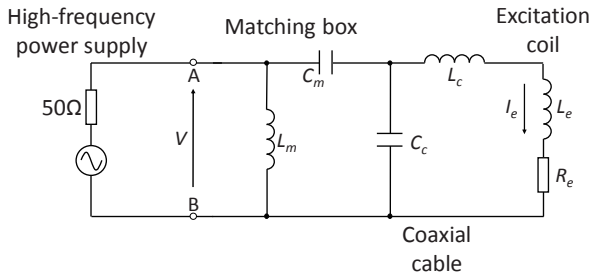

Fig. 2 Simplified equivalent circuit.

3. Experimental results

3.1 Characteristics of resonant circuit

We evaluated the changes in impedance locus by varying the resonant circuit parameters. Fig. 3 shows the measured impedance locus when the inductance of excitation coil L_e was changed. In the resonance band, the impedance locus starts near the imaginary axis and moves in a clockwise direction with increasing frequency before returning to the imaginary axis. To maximize the power factor and minimize the reflected power, the impedance locus should pass through the matching point (50+j0 Ω) and a matched frequency should be chosen. For example, the impedance locus of a 3×2-turn coil should be reduced and a 10×2-turn coil should be expanded for impedance matching, as shown in Fig. 3.

The size of the impedance locus was evaluated from the maximum value of the real part impedance $\mathrm{Re}\{Z\}$. Fig. 4(a) shows that the size of impedance locus reduces with increasing inductance. Fig. 4(b) shows the relationship between inductance of the excitation coil and the resonant frequency f_r. A diamond indicium was calculated value that was obtained from the impedance locus by Eq. (1). The experimental value of the 50 mm prototype was plotted using a filled circle. We define the resonant frequency f_r as the frequency at which the phase of impedance becomes 0 from a positive value. When the phase did not equal 0, the minimum frequency was adopted and plotted using an unfilled indicium. When calculating the impedance locus by Eq. (1), the measured frequency characteristic of AC resistance of the 50 mm prototype was applied to the resistance R_e. As for the calculation value in Fig. 4(a), there is the variation to approximate curve due to the resistance frequency characteristic that has the measurement error. The difference between the calculated value and experimental value, shown in Figs. 4(a), 5(a) and 6(a), was due to the parasitic capacitance between the internal wiring and the metal housing of the matching box.

Fig. 4 shows that the trend of the calculated value agrees with that of experimental value. The resonant frequency f_r is inversely proportional to the inductance of the excitation coil (Fig. 4(b)). Coils with a small inductance (a small number of turns) have higher operating frequencies but weaker magnetic fields. Conversely, a coil with large inductance (a large number

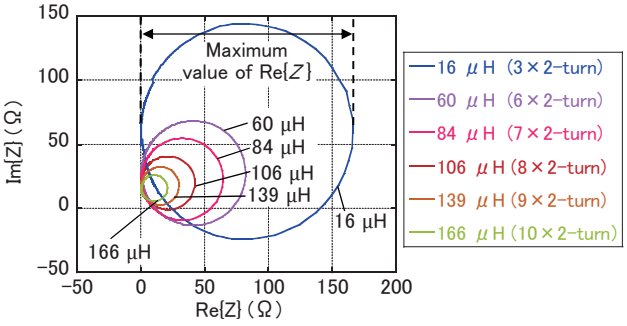

Fig. 3 Measured impedance locus.

of turns)have a stronger magnetic field but a lower operating frequency. There is therefore the trade-off relationship between frequency f_r and magnetic field strength H.

Fig. 5(a) shows the relationship between matching capacitance C_m and the size of the impedance locus. Fig. 5(b) shows the relationship between matching capacitance C_m and resonant frequency. As shown in Fig.5, the trend of the calculated value qualitatively agrees with that of the experimental value. Resonant frequency f_r increases with decreasing C_m (Fig. 5(b)). However, an increasing f_r brings increasing AC resistance R_e. Eq. (2) shows that excitation current I_e decrease with increasing R_e; the magnetic field becomes weaker. Therefore, there is also a trade-off between frequency f_r and magnetic field strength H.

Fig. 6(a) shows the relationship between matching inductance L_m and the size of the impedance locus. As shown in Fig. 6, the trend of the calculated value qualitatively agrees with that of the experimental value. The impedance locus expands monotonically with increasing L_m. Fig. 6(b) shows the relationship between matching inductance L_m and resonant frequency f_r. In the change from L_m = 4.09 μH to 5.24 μH, the change of experimental f_r is only -3.8 kHz because the influence of L_m on f_r is small. This is in contrast to the significant changes in impedance locus (Fig. 6(a)). It is found that L_m is uniquely determined for impedance matching at the

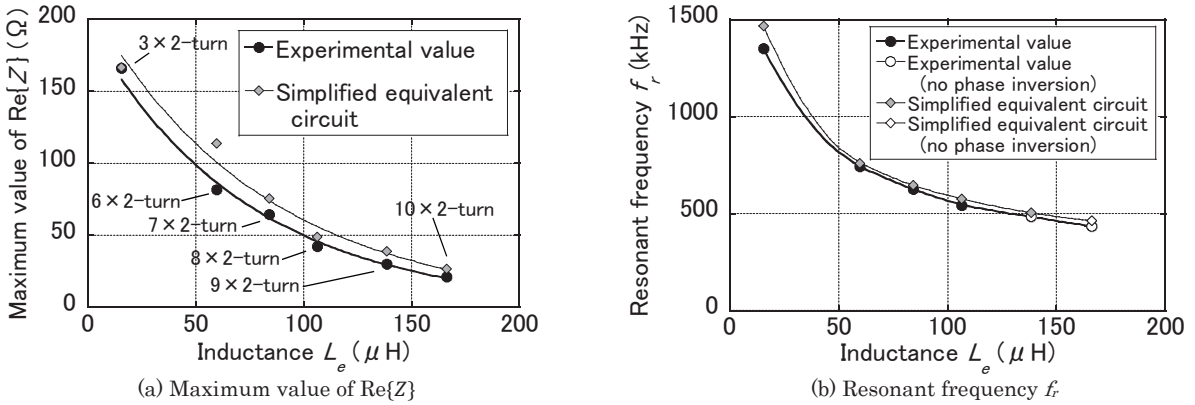

(a) Maximum value of Re{Z}　(b) Resonant frequency f_r

Fig. 4 Relationship between inductance of excitation coil and resonant characteristics.

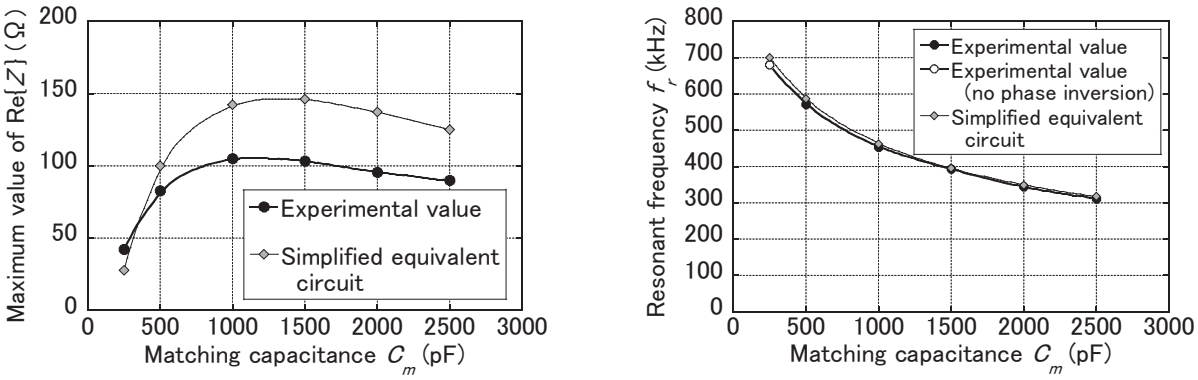

(a) Maximum value of Re{Z}　(b) Resonant frequency f_r

Fig. 5 Relationship between matching capacitance and resonant characteristics.

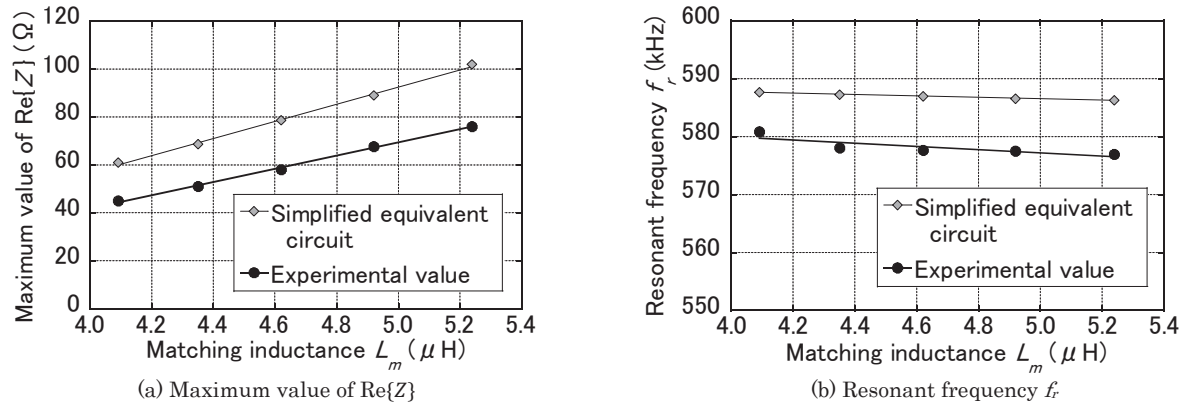

(a) Maximum value of Re{Z}　(b) Resonant frequency f_r

Fig. 6 Relationship between matching inductance and resonant characteristics.

time of choosing L_e and C_m. Therefore, we adjust the matching inductance L_m for impedance matching.

Figs.4, 5 and 6 show the characteristic of the equivalent circuit qualitatively agrees with that of the experimental resonant circuit with the 50mm prototype. Therefore, we show that the simplified equivalent circuit is appropriate to describe circuit characteristics and the above resonant circuit characteristic is applied to other excitation coils, such as a full-scale applicator.

3.2 Guideline for optimizing circuit parameters

According to our investigation of resonant circuit characteristics, we found that there is a trade-off between magnetic field strength, resonant frequency. Therefore, we consider that there is an optimal combination of the resonant circuit parameter. In this section, we show the guideline for examining the optimal combination of circuit parameters that maximizes the estimated heating index while maintaining matching conditions by changing various parameters.

We show the optimization procedure below. Firstly, we set L_e and C_m. After that, impedance locus was adjusted to the matching point with L_m. Secondly, a fixed input power was applied; in this paper 180 W. Thirdly, the excitation current I_e and frequency f_r were measured and magnetic field strength H was calculated. Fourthly, the estimated heating index was evaluated from the product of frequency f and magnetic field strength H. This series of flow was executed until the maximum value of estimated heating index was found.

The multiplier of f and H differs depending on the type of heating mediator. For instance, the SAR of an electrical conductor is proportional to f^2H^2, that of a magnetic fluid is proportional to fH^2 [3) 6)], and that of a bulk magnetic material is proportional to $fH^{1.5\text{-}2.3}$ [7) 8)]. We evaluated f^2H^2 for an electrical conductor and fH^2 for a magnetic fluid or bulk magnetic material.

We applied the above-described procedure to the 50 mm prototype and acquired I_e, H and f_r in a plurality of combinations of circuit parameters. Fig. 7(a) shows the relationship between matching capacitance and excitation current when the input power is 180 W. The excitation current having a larger number of turns is smaller when C_m is greater than 500 pF. Coils having a larger number of turns can generate a strong magnetic field even though the exciting current is small (Fig. 7). However, although increasing the number of turns increases the strength of the magnetic field, the frequency is reduced as a result (Fig. 8). Additionally, although it is better for a stronger magnetic field to increase C_m (Fig. 7(b)), an increase in C_m reduces the frequency (Fig. 8).

Figs. 9 and 10 show the estimated heating index for each type of heating mediator. The optimal combination of parameters in terms of maximizing the estimated heating index varies depending on the heating mediator. This is because the influence of frequency and magnetic field strength on SAR differs depending on the mediator.

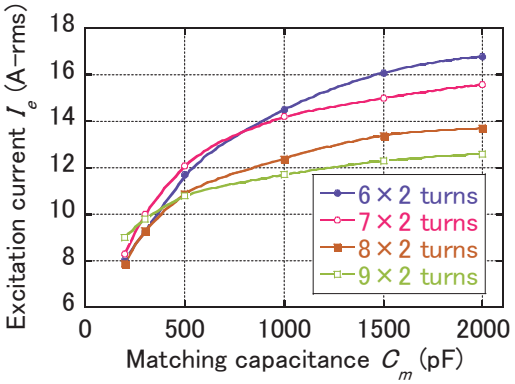

(a) Excitation current I_e

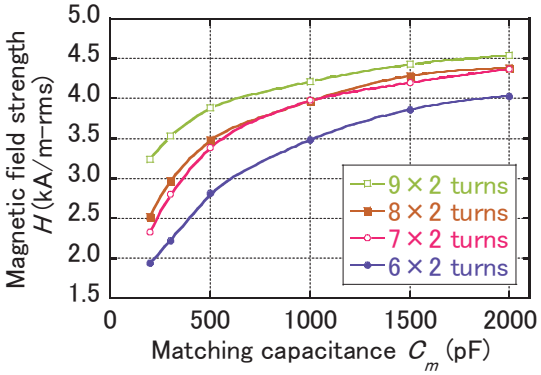

(b) Magnetic field strength H

Fig. 7 Excitation current and magnetic field strength when input power is 180 W.

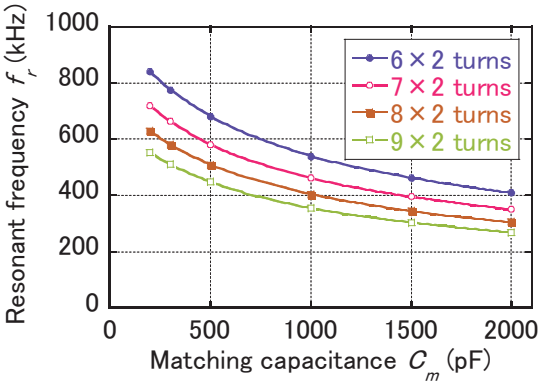

Fig. 8 Relationship between matching capacitance and resonant frequency.

The SAR of electrical conductors is proportional to f^2H^2 and is significantly affected by frequency. Hence, the combination using C_m = 500 pF is optimal because of the higher frequency. The SAR of a magnetic fluid or bulk magnetic material is proportional to fH^2 because magnetic field strength has a significant impact on their SAR. Hence, the combination using C_m = 1000 pF is optimal because of the stronger magnetic field. It was found that the optimal combination of the resonant circuit was uniquely determined for each of the heating mediators. We consider that this guideline is helpful for designing a full-scale and high-estimated heating index operation MHT applicator.

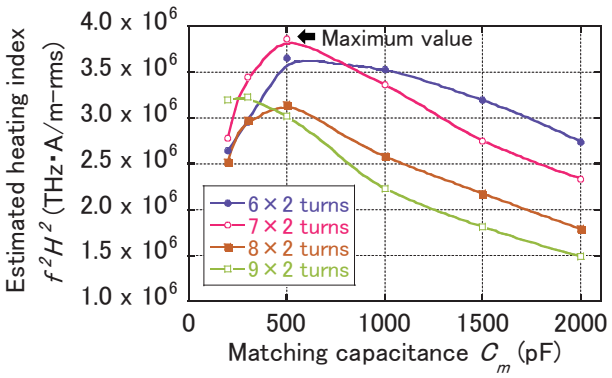

Fig. 9 Estimated heating index for electrical conductor.

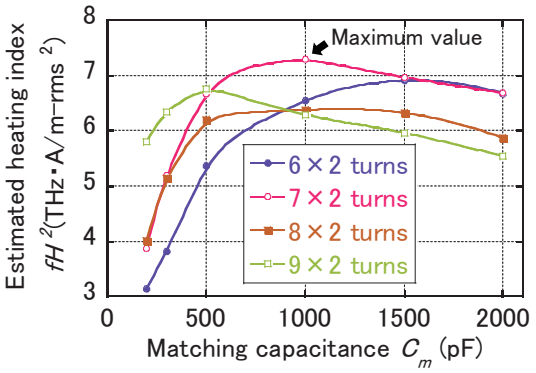

Fig. 10 Estimated heating index for magnetic fluid and bulk magnetic material.

3.3 Experimental demonstration of magnetic field distribution

To demonstrate the validity of the magnetic circuit type magnetic field generator, we measured the magnetic field distribution with a pickup coil. The pickup coil was manufactured with 11 turns of a polyurethane copper wire (φ = 0.12 mm). The cross-sectional area of the coil was 1 cm^2. The magnetic field strength was obtained by measuring the effective value of the induced electromotive force of the pickup coil. Furthermore, electromagnetic field analysis was performed using the finite element method (ANSYS, Maxwell ver.12). The number of turns of the exciting coil was 7×2, the exciting current was 8.3 A RMS, and the operating frequency was 450 kHz. The experimental magnetic field strength was 2.5 kA/m RMS at the center point of the 50 mm prototype (x=0, y=0, z=0) and the analytical value was 2.3 kA/m RMS, thereby demonstrating good agreement with the experimental value. The magnetic field strength was normalized by the center point to investigate distribution.

Fig. 11 shows the surface distribution of the magnetic field strength in the zx-plane, which was obtained by analysis, and the experimental line distribution of the magnetic field. The magnetic field has uniformity to within ±5% between magnetic poles. Figs. 12 and 13 show the surface distribution in the xy-plane and yz-plane and the experimental results. As shown in Figs. 11 to 13, the

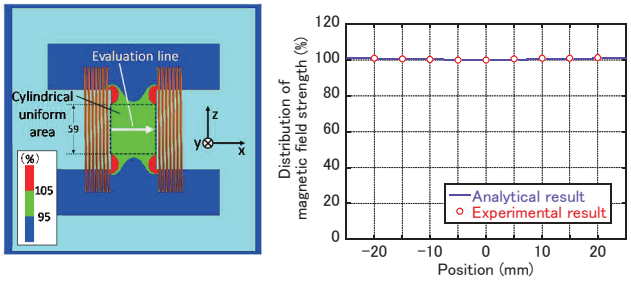

(a) zx-plane distribution (b) Line distribution along x-axis

Fig. 11 Magnetic field distribution by experiment and analysis (zx-plane).

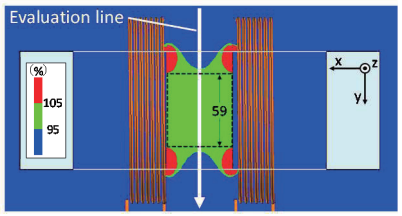

(a) xy-plane distribution

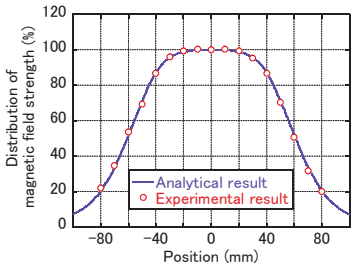

(b) Line distribution along y-axis

Fig. 12 Magnetic field distribution by experiment and analysis (xy-plane).

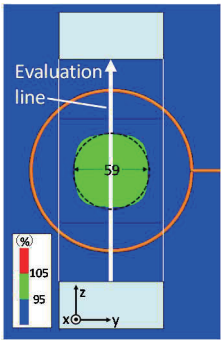

(a) yz-plane distribution

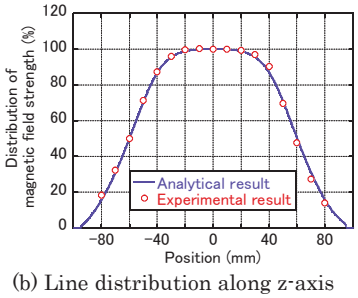

(b) Line distribution along z-axis

Fig. 13 Magnetic field distribution by experiment and analysis (yz-plane).

experimental results agree with the analysis results for any axis. A homogeneous magnetic field is distributed in a cylindrical shape. The diameter of the cylindrical area is 59 mm, and the volume is 0.14 L. Assuming that measurements of the 50 mm prototype are scaled up 6 fold to human body size, the volume of uniform magnetic field becomes 30 L (≈ 0.14 L × 6^3). This meets the 10 L requirement. Thus, this design of magnetic circuit type magnetic field generator is appropriate for MHT applications.

4. Conclusion

We fabricated a 50 mm prototype with a magnetic circuit and evaluated the characteristics of the resonant circuit. By measurement of resonant circuit characteristic and equivalent circuit analysis, we show the generality of the resonant circuit of the 50 mm prototype. Therefore, the resonant circuit characteristic that was shown in this paper can be applied to other excitation coils, such as a full-scale MHT applicator. It was found that there is the trade-off relationship between frequency f_r and magnetic field strength H. The guideline for optimizing resonant circuit parameters was suggested by assuming that the product of frequency and magnetic field strength equates to the estimated heating index.

We applied this guideline to the 50 mm prototype. The 7×2-turn coil (84 μH), C_m = 500 pF (for electrical conductor) and C_m = 1000 pF (for magnetic fluid or bulk magnetic material) is optimal for the 50 mm prototype. We found that the optimal combination is uniquely determined. We consider that this guideline can be applied to a full-scale MHT applicator, because this guideline has generality.

Furthermore, we evaluated the distribution of magnetic field strength using the 50 mm prototype. It was demonstrated that a 50 mm prototype can generate a 0.14-L volume uniform magnetic field that has uniformity to within ±5%. The validity of the magnetic circuit type magnetic field generator was experimentally confirmed.

The feasibility of the a full-scale MHT applicator was increased by the guideline for high-estimated heating index operation and the experimental demonstration of magnetic field homogeneity in the magnetic circuit type magnetic field generator.

Acknowledgement

Part of this work was supported by JSPS KAKENHI Grant Number 16K13666.

References

1) Y. Tanaka: Hyperthermia Gan Onnetsuryouhou Guidebook (in Japanese), Japanese Society for Thermal Medicine, p.4(Sinryou Bunko, Kobe, 2008)
2) T. Yoshioka, T. Nakagawa, M. Horiki, S. Seino, T. A. Yamamoto, T. Gondo, T. Hashimoto, M. Ohori, and M. Abe: *J. Magn. Soc. Jpn.*, 35, 330-334 (2011)
3) E. A. Périgo, G. Hemery, O. Sandre, D. Ortega, E. Garaio, F. Plazaola, and F. J. Teran: *Applied Physics Reviews 2*, 041302 (2015)
4) M. Horiki, T. Nakagawa, T. Yoshioka, S. Seino, T. A. Yamamoto, M. Abe: *J. Magn. Soc. Jpn.*, 35, 22-26 (2011)
5) A. Jordan, R. Scholz, K. Maier-Hauff, M. Johannsen, P. Wust, J. Nadobny, H. Schirra, H. Schmidt, S. Deger, S. Loening, W. Lanksch, R. Felix: *J. Magn. Magn. Mat.*, 225, 118-126 (2001)
6) A. Jordan, R. Scholz, P. Wust, H. Fähling, R. Felix: *J. Magn. Magn. Mat.*, 201, 413-419 (1999)
7) M. A. Laughton, M. G. Say: Electrical Engineer's Reference Book, p.2/13 (Newnes, Oxford, 2003)
8) W. Tong: Mechanical Design of Electric Motors, p.376 (CRC Press, Boca Raton, 2014)
9) M. Takahashi, T. Nakagawa, S. Seino, T. A. Yamamoto: *J. Magn. Soc. Jpn.*, 38, 102-106 (2014)

Received Dec. 12, 2017; Revised Jan. 22, 2018; Accepted Feb. 07, 2018

Journal of the Magnetics Society of Japan

Vol. 42 No. 3 (通巻第 297 号) 2018 年 5 月 1 日発行

Vol. 42 No. 3 Published May. 1, 2018
by the Magnetics Society of Japan
Tokyo YWCA building Rm207, 1–8–11 Kanda surugadai, Chiyoda-ku, Tokyo 101–0062
Tel. +81–3–5281–0106 Fax. +81–3–5281–0107

Printed by JP Corporation Co., Ltd.
2–3–36, Minamikase, Saiwai-ku, Kanagawa 212–0055
Advertising agency: Kagaku Gijutsu-sha

発行：（公社）日本磁気学会 101–0062 東京都千代田区神田駿河台 1–8–11 東京YWCA会館 207 号室
製作：ジェイピーコーポレーション 212–0055 神奈川県川崎市幸区南加瀬 2–3–36 Tel.（044）571–5815
広告取扱い：科学技術社 111–0052 東京都台東区柳橋 2–10–8 武田ビル 4F Tel.（03）5809–1132